THE DIRECT IMAGING SEARCH FOR EARTH 2.0

Claire Marie Guimond

Master of Science

Department of Earth & Planetary Sciences

McGill University

Montreal, Quebec

July 6, 2018

A thesis submitted to McGill University in partial fulfillment of the requirements of the degree of Master of Science

DEDICATION

This work goes out to my blood sisters, Grace and Laura, and to any other sisters reading it, particularly those identifying with the queer, BIPOC, and/or disability communities.

ACKNOWLEDGEMENTS & CONTRIBUTIONS

All research was conducted on unceded territory of the Kanien'kehá:ka nation. This project has been supported by the McGill Space Institute, the Technologies for Exo-Planetary Science training program, and by an NSERC Discovery Grant awarded to N. B. Cowan. Completing my degree would not be possible without the tolerance of my supervisor, N. B. Cowan.

This thesis is centered on a manuscript accepted for publication in the Astronomical Journal, which was co-authored by my supervisor, Prof. N. B. Cowan. The experiment was designed by NBC and CMG. CMG wrote the Python code for the model, executed the experiment, and designed figures. Analysis of the results and writing of the manuscript text (chapter 3) was performed by CMG with guidance and editorial help from NBC. Chapters 1–2 were written by CMG, and in chapter 4, NBC assisted CMG with mathematical brainstorming. Prof. Andrew Cumming gracefully served as the examiner of this thesis.

ABSTRACT

Direct imaging is the next-generation technique of exoplanet science. It is likely the best way to characterize the atmospheres of Earth-size exoplanets in the habitable zones of Sun-like stars. Future space missions such as LUVOIR and HabEx are designed to find these Earth twin planets, but the cardinal purpose is to characterize them, and a search using direct imaging is not necessarily the fastest way. Given a pale white dot at the right projected separation and brightness to be an Earth twin, what are the odds that it is, in fact, an Earth twin? We show that the planetary false positive rates of these searches are prohibitively high, and always greater than one in two. The majority of culprits will be big, dark planets with large radii and low albedos. Going forward, easing the the false positive rate would be helped by alternative methods to discriminate Earth twins—photometric phase variations, spectroscopy, or synergies with other detection methods.

ABRÉGÉ

L'imagerie directe est la technique de prochaine génération de la science des exoplanètes. C'est fort probablement le meilleur moyen de caractériser les atmosphères des exoplanètes terrestres dans les zones habitables des étoiles semblables au Soleil. Les futures missions spatiales telles que LUVOIR et HabEx sont conçues pour trouver les planètes jumelles de la Terre, mais le but cardinal est de les caractériser. Détecter ces planètes par imagerie directe n'est pas nécessairement le moyen le plus rapide. Étant donné un point blanc pâle avec une séparation projetée et une luminosité comparable à celles de la Terre, quelles sont les chances qu'il s'agisse, en effet, d'une jumelle terrestre? Nous montrons que le taux de détection de faux positifs pour les sondages qui utiliseront la méthode d'imagerie directe est dangereusement large et toujours supérieurs à un sur deux. La majorité de celles-ci seront de grandes planètes sombres avec de grands rayons et des albédos bas. Ainsi, dans la saga de la caractérisation des jumelles de la Terre, un albédo non-contraint sera un ennemi coriace à vaincre.

TABLE OF CONTENTS

LIST OF TABLES

LIST OF FIGURES

Preface

This thesis documents the attempt to find Earth-like planets in the habitable zones of Sun-like stars. It centers on a manuscript accepted for publication in the Astronomical Journal [57], which is contained entirely in chapter 3. Chapter 1 presents a layman's overview and justification of the work, and chapter 2 a formal literature review. Chapter 4 connects several unpublished, incubating research questions. The thesis is concluded laconically with a summary in chapter 5.

Chapter 1
Earth twin planets and why we look for them

The fancy of other planets looking like ours has struck minds on Earth for lifetimes, but the science institution has regarded them for meager decades. Our nearest enticed us until we probed her with radio waves. Then in 1958 we learned [84] that Venus was not the teeming jungle of fiction: too hot to be hospitable, surely uninhabited. Decades passed, then baited again when we witnessed [132] inaugurally an exoplanet in another star system. A hundred thousand times as far away, and many times harder to penetrate. Not until decades further—our future—do humans start constructing devices to locate our real sister world.

We are tenderfooted just like those mid-century thinkers [110] who deliberated life on Venus and in the solar system. Rather than just eight alien planets to look at, however, we have 3758 (as of April 13, 2018). We now know that planets span an immense diversity of configurations, unpredictable by our own solar system. We can use statistical tools to examine planets more generally. We know that some planets are Earth-sized, and we hope to learn whether some are truly, this time, our interstellar twins.

This work heralds the observational study of such Earth-like exoplanets, or as we refer to here, Earth twins. Today we conduct research to inform missions in the future: we anticipate that by the 2030s, technology will have advanced enough to measure from space the climates of Earth twins. Therefore we aim to predict and discuss the outcomes of nominal space-based missions.

The work is necessary to the institution because these missions will be expensive; of course we should be maximizing scientific return. If we claim that a proposed mission will be capable of obtaining a given measurement, then we would be wise to simulate these data well in advance, and demonstrate that their analyses would be sufficiently conclusive. Poorly-strategized data acquisition could set the research community back decades. Perhaps the reader would be surprised, then, to learn that extant Earth-searching simulations of this sort [122, 121, 123] neglect details that could confuse analysis. I will show what searching a realistic universe might reveal to us.

1.1 Detailed rationale

In figure 1–1, I show every exoplanet around a Sun-like star with a measured planetary radius and distance from their star. The familiar solar system planets are overlain—their locations may seem like a mistake. The architectures of exoplanets do not look like our solar system. This is partly due to observer bias—current detection techniques are less sensitive to Earth, Venus, and Mars twins—but the more we study exoplanets, the more it seems that our home is an outcast.

The message is simply: there is an enormous untapped diversity of small planets. The most common planet size seems to be larger than Earth but smaller

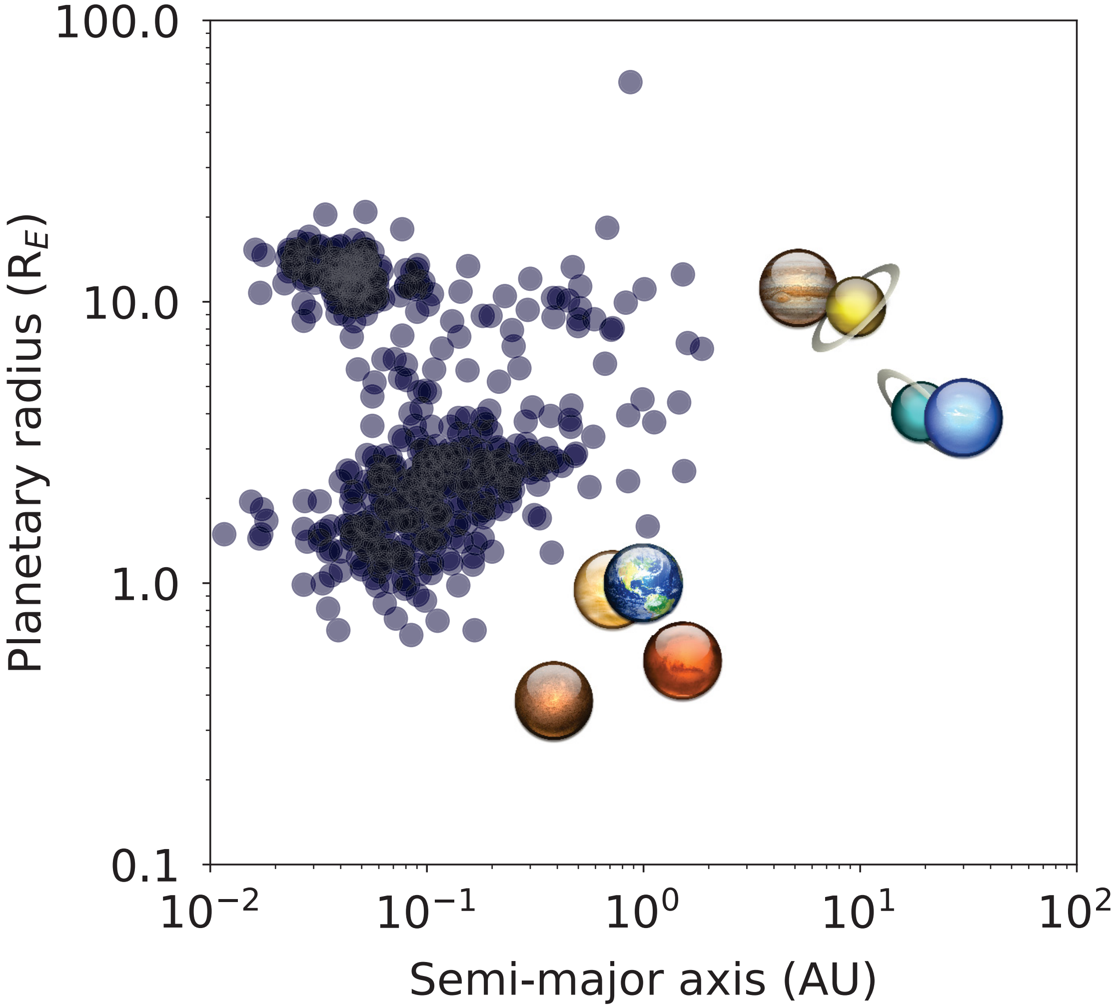

Figure 1–1: All confirmed (exo)planets around solar-mass stars with known radii and semi-major axes. Based on data retrieved from `exoplanets.eu` on March 22, 2018. Solar system planets are represented by icons.

than Neptune.[1] There are no solar system analogs to which we can send probes. One might conceptualize either a scaled up Earth, a rocky planet with relatively thin atmosphere; or otherwise a scaled down Neptune, with a rocky core but a thick H/He envelope. The precise division between them is debated [80, 129, 108, 78, 50, 18], as we will see in the next chapter.

The other axis in figure 1–1 is the semi-major axis of the orbit. This separation sets the space environment of the planet; primarily, the amount of sunlight received, which in turn serves as a low-order control on global climate. A scientist searching for Earth 2.0 would therefore care about this parameter. An often-heard term packing this concept is the *habitable zone*. Reductionistically, too close to the star the oceans boil away; too far, they freeze. Again, there is regular debate on where exactly the habitable zone boundaries lie [95, 136, 91, 71, 72, 120, e.g.].

It is a NASA decadal objective to search for terrestrial planets [52]. As I have just motivated, a true Earth twin is defined by its similarity to Earth in both radius and semi-major axis, but this region of parameter space is difficult or impossible to probe with current detection technology. Thus I bring in the next-generation technology of *direct imaging*. As the name implies, this method spatially resolves planet-light from starlight, compared to the other detection methods which tease periodic signals indirectly. Direct imaging is the only way to see atmospheres of habitable planets around Sun-like stars.

[1] `exoplanetarchive.ipac.caltech.edu`

An eventual goal is to study the composition of these planets' atmospheres, which is possible by breaking the integrated white light into a spectrum, looking for absorption features. This follows the same principle as the satellite remote sensing of Earth, but on an obviously rougher spatial resolution. The crux is that these spectroscopic observations require month-long exposure times, orders of magnitude longer than broadband imaging [107]. So we must be selective with our spectroscopy targets. The preparatory, diagnostic step is to first image the planet with broadband light.

With photometric direct imaging, we obtain two pieces of data: the relative position (between the planet and its host star), and the relative brightness. We are not measuring radius nor semi-major axis unambiguously. Then, we cannot tell right away if a detected planet is an Earth twin.

You can measure the distance from the planet centroid to the star with a ruler. However, this measurement is not the semi-major axis but the projected separation, as the image is a 2D projection of a 3D orbit. This is a degeneracy: one cannot ascribe a unique orbit to a single snapshot of a planet (figure 1–2). With multiple observations at different epochs, the orbit might be constrained and eventually known. Another route to breaking this degeneracy is to target planets that have previously been detected with indirect techniques, with orbits already constrained.

The relative brightness refers to the ratio of starlight to reflected planet-light. Earth twins will *not* be spatially resolved, but their signals span several pixels due to the diffraction limit. A smaller planet would translate to less-bright pixels.

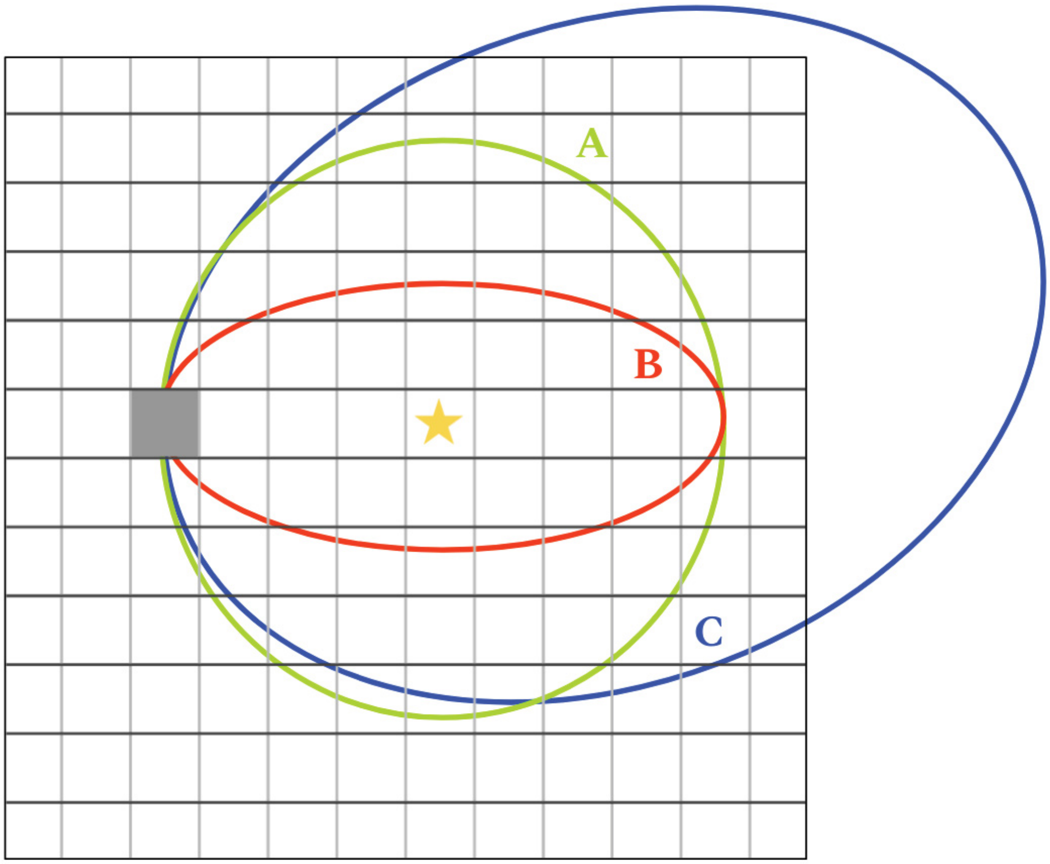

Figure 1–2: *Cartoon of the orbit degeneracy.* With a single direct imaging, snapshot, we cannot tell whether the detected planet (grey pixel) follows an orbit that is circular (A), inclined (B), eccentric (C), or some combination of the latter two. One pixel is shown for pedagogy, but note that the diffraction limit dictates that the planetary signal actually covers multiple pixels. Pixel size is not to scale.

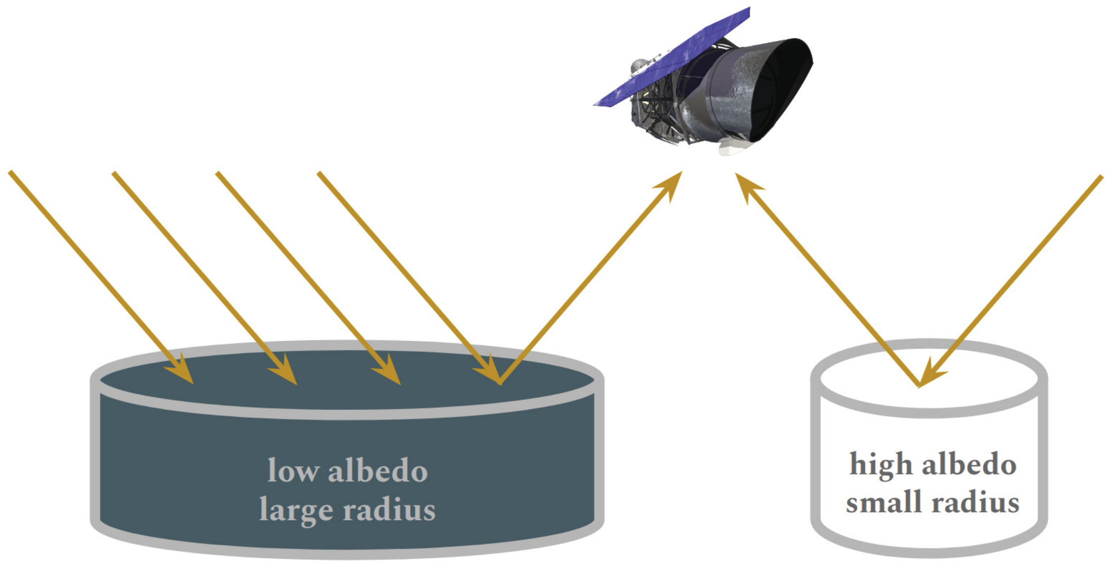

Figure 1–3: *Cartoon of the radius-albedo degeneracy.* Two different-sized disks receive the same flux density, but the small disk reflects 100% of incoming rays, and the large one reflects 25%. From the point of view of the telescope, the signal from both disks is identical.

Actually, four components go into this brightness: radius, albedo, semi-major axis, and orbital phase. In a single snapshot, they are degenerate with each other. We can measure semi-major axis if we spend more observations, although ultimately we reach stalemate trying to distinguish big objects from shiny objects (figure 1–3).

So, at risk of repeating myself, it is necessary that we are able to discriminate between potential targets, and choose the targets that give us highest priority science. Because of degeneracies between radius and albedo, and between projected separation and semi-major axis, there are always going to be some planets that look Earth-like from observation, but are in fact "false positives" for Earths.

Therefore it would be wise to have an estimate of the false positive rate: given a new pale dot in the sky, how likely is it that you are seeing an Earth-like planet? This question, answerable by a scalar quantity, summarizes the work.

1.2 Research objectives

In this research program, I perform the following:

- review the literature on the distribution, detection, and characterization of potentially Earth-like exoplanets;
- using Monte Carlo methods, predict the efficiency of a nominal future space mission at finding these Earth twins;

and

- contemplate the possible improvements in recognizing Earth twins using photometry.

Chapter 2
Review of the literature

Terrestrial exoplanets are still obscure among this nascent body of exoplanet research. Even the weightiest works have relatively few citations, so this review will not be choosy. We come across lessons from the statistical distribution, detection, and characterization of exoplanets.

2.1 Distributions of Earth twins

I fixate here on the lowest-order demographics of planets. Planets, like asteroids and bacteria, are sorted taxonomically into classes based on observables, in particular radius, R_p, and period, P.[1] Thus we care about probability density functions; e.g., in the form $\mathrm{d}N/\mathrm{d}R_p = f(R_p)$. I will allude to these functions' behaviour around Earth, and discuss what has been inferred about the occurrence rate of Earth-like planets in the habitable zone of Sun-like stars—or as they will be referred to onwards, Earth twins.

Filling in the right-hand sides of the equations is complicated by a selection effect, whereby some regions of parameter space are more readily detectable than others [33]. Writing distribution functions is also complicated by heavy measurement error on the actual retrieval of these properties. Despite this, our

[1] Knowing period is equivalent to knowing semi-major axis, given the stellar mass, via Kepler's third law.

sample breadth and instrument precision are now good enough to confirm the compelling richness of small planets [7].

Exoplanet demographics inform the work two-fold: (i) a planet's signal strength and thus its detectability depends on a particular set of properties for a given detection method; and (ii) the underlying planet occurrence rate dictates what planets are available to be detected in the first place.

2.1.1 The new planet regimes

At this present inflection point in the exoplanet discovery rate, the known diversity of exoplanets is repeatedly recast. Comparative exoplanetology benefits from a robust classification system [69, 25, 80]. While some may write off this pursuit as stamp-collecting, it is actually very important, Sir Rutherford, to have a taxonomic understanding of the $\sim$4000-and-counting known planets.

This work cares about class boundaries because it seeks to quantify the false positive rate of Earth twin searches. To tally the yield of false positives, we must systematically distinguish Earths from other flavours of planets. Ideally, attributing Earth-likeness would consider exoplanetary climate, which is inferred from models [65]. Yet we do not have a real sense of climate prognostication. It is unclear if the best predictors are semi-major axis and radius, or alternatively semi-major axis and mass—there could be a location in either plane occupied by many, variously-habitable planets. Perhaps some higher-order parameter, such as initial water inventory or surface gravity, serves as the best predictor of climate state.

I nonetheless adopt R_p and P as the currently-most-feasible, lowest-order predictors of Earth-likeness. The transiting planets detected by the *Kepler* mission form a useful sample because their radii and periods have been measured.

Recently, Kopparapu et al. [70] proposed a classification scheme stemming from the notion that planet size is strongly controlled by volatile inventory [80]. We repeat their categories here. Planets are sorted according radius and insolation: rocky (0.5–1.0 $R_\oplus$), super-Earths (1.0–1.75 $R_\oplus$), sub-Neptunes (1.75–3.5 $R_\oplus$), sub-Jovians (3.5–6.0 $R_\oplus$) and Jovians (6–14.3 $R_\oplus$) for the former; for the latter, cold, warm, and hot. Due to the non-linearities of greenhouse gas forcing and gravity effects, the temperature classifier depends on the size classifier. Rocky planets are considered warm if they receive between 1.0 and 0.28 times Earth's insolation (365–948-day periods for Sun-like stars), while super-Earths require slightly more sunlight.

This updates a scheme developed from early *Kepler*, which sorted the quaint 1235 planet candidates by radius into Earths, super-Earths, Neptunes, and Jupiters [13]. The addition of the sub-Neptune class reflects our increasing (in)comprehension of the transition from Earth to Neptune analogs.[2]

The broad intentions behind planet classes are themselves congruent across the literature. We have small planets dominated by iron and silicate rock, with

[2] Plus, pushing the term "sub-Jovian" to replace the rigid "Neptune" is nice because it implies that the transition from Neptune analogs to Jovian analogs is also more subtle and enigmatic than we thought.

thin atmospheres. These encompass Earth, Venus, and Mars twins. Larger radii mean more significant atmospheres, made of light gases and/or astrophysical ices, but still atop this fundamental iron-silicate core. Even larger than this, and the planet is essentially driven by its volatile envelope. The dominant paradigm for sub-giants is that larger radii generally mean thicker envelopes, as opposed to enormous cores. This is supported by core-accretion theory in that bare $10M_\oplus$ planets are difficult to build [80].

Earth-Neptune transition. For the left side of the radius distribution, the region relevant to the work, is informed by the planetological transition from thinner to thicker atmospheres. If this transition is sharp with respect to radius, then we will want to be very careful about distinguishing Earth twins from super-Earths based on radius retrieval. Indeed, radius alone may be suggestive of the H/He envelope fraction [80].

The radius distribution in this domain is bimodal, with a distinct paucity of planets between 1.5 and 2.0 $R_\oplus$ [50, 137]. This hints at a dividing line backed by observation: planets near the lower mode have rocky compositions, while planets near the upper mode are dominated by gaseous envelopes. This "radius gap" is probably attributable to some unknown atmospheric loss process(es)—such as photoevaporation [93], hydrodynamic escape [78], or core-powered mass loss [55]—or alternatively, gas-poor formation [77].

Rogers [108] preempts this radius gap using density constraints from planets with measured radii and masses. Empirically, planets $1.6R_\oplus$ and above are not dense enough to be an all-iron-silicate sphere, hence significant gaseous envelopes fill out their radii. Weiss & Marcy [129] also use mass and radius observations to find a density-radius inflection point at 1.5 $R_\oplus$, indicating gaseous envelope buildup. Both these observed upper radius limits agree with an accretion model that produces upper and lower limits of 2.0 $R_\oplus$ and 1.5 $R_\oplus$ for the transition region [80]. Another model [78] ponders atmospheric loss driven by UV radiation and finds a rocky upper limit of 1.8 $R_\oplus$. Chen & Kipping [24] imply that the transition occurs at a quite-small radius of 1.3 $R_\oplus$, on the basis of an inflection point in an empirical mass-radius relation, although this ignores subtleties between Earth and super-Earth regimes.

2.1.2 Period distributions

Earth twins orbit farther out than the bulk of *Kepler* detections. Current catalogs[3] list a set of larger radial velocity planets beyond 1 AU, but these planets would not be Earth-like, and we know their masses, not their radii. Where the radius distribution around $R_p \sim 1\,R_\oplus$ is bimodal and physically-motivated as such, the distribution of longer-period planets can be broadly described as flat in logarithmic space. That is, $\mathrm{d}N/\mathrm{dln}\,P \propto P^{\sim 0}$, if one takes a power law distribution as a prior [127, 96, 34, e.g.].

Relaxing the assumption of a power law has hinted at longer periods being more common (in logarithmic bin widths) [61]. If one includes planets with very short periods (<3 days), then $\mathrm{d}N/\mathrm{dln}\,P$ shows a peak very close to the star, which

[3] i.e., `exoplanets.eu, exoplanetarchive.ipac.caltech.edu`

represents an enigmatic class of “hot” planets [33]. At the least, there is no fully-explained reason why we would expect the universe to be biased towards or away from $P{\sim}1$ year. However, one potential argument lies in the pile-up of eccentric Jupiter-mass planets close to 1 AU:[4] this would preclude Earth-mass planets from long-term residency in the habitable zones of such systems.

2.1.3 Classifying habitability

Sorting planets based on radius and period only matters for us if radius and period are the dominant parameters governing planetary climate, and hence Earth-likeness.

Habitable zones represent our attempts to predict where an exoplanet could feasibly support liquid surface water [64, 71]. This would be set primarily by mean surface temperature, which in turn depends on a number of hard-to-constrain parameters such as winds [72] and clouds [134]. Not enough attention is given to the H_2O-budget consequences from geological-scale history of atmospheres [136, 56] and planetary interiors [91]. Hence habitable zone boundaries are estimated from planetary climate models. Yet habitability cannot really be “measured”, and meanwhile our sample size of confirmed habitable planets rests at one.

This has been the common way of judging potential Earth-likeness in lieu of direct observability; however, of course, it is risky to impress binary states (i.e., habitable/not habitable) based on models alone. In theory, we can infer Earth twins’ climatic states by measuring how photons interact with materials in a

[4] Based on data from `exoplanets.eu` retrieved April 2018

planet's atmosphere and surface. JWST is designed to detect biosignatures—observable signs of biological metabolism [109]—in the atmospheres of super-Earths [113]. Several gold-standard biosignatures are proposed, in particular the co-detection of O_3 and CH_4 [83, 101], but planetary controls for false positives will be needed to evaluate the robustness of any biosignature [106]. Stark et al. [122], for instance, posit the detection of atmospheric H_2O as a defining trait for Earth-likeness, but H_2O vapour is common in all sorts of atmospheres [62].

Stellar spectral type is also an important factor in habitability [79]. This is why I only consider planets around "Sun-like" stars when discussing Earth twins: G-, and sometimes F- and K-dwarfs. Although lower-mass M-dwarfs are more common stars, their systems have contested livability: habitable zones scale inward in semi-major axis due to the dimmer stellar output, so an M-dwarf's planet receiving the same stellar flux as Earth would be exposed to very harsh UV radiation [79]. Further, these planets are close-in enough to become synchronously rotating [4]. Our understanding of global climate in this tidal-locking regime is poor, but at the least, such climates should have precipitous stability [68].

Formal definition of an Earth twin. While any of these assumptions may be reasonable, they remain unproven. The most reasonable way to define Earth twins with our current knowledge is based on chosen values of radius and semi-major axis. For instance, this work adopts one nat, centred on Earth values, as the box-width of either parameter.

2.1.4 Earth twin occurrence rates

As exemplified by the *Kepler* mission objective, there is active research in determining the fraction of stars that harbour Earth-size planets in (or at least near) the habitable zone [14]. Occurrence rates are expressed as the expected number of planets per star, η, usually for some range of periods, radii, masses, etc. One can also report the occurrence rate *density* of planets: the expected number of planets per star per unit period per unit radius, where these units are given in their logarithms. This joint probability density function is notated by $\Gamma_\oplus$, and is analytically equal to $\mathrm{d}^2N/\left(\mathrm{d}\ln P\,\mathrm{d}\ln R\right)$ evaluated at $P = 365$ days and $R_p = 1\ R_\oplus$, or conversely,

$$\eta_\oplus = \Gamma_\oplus \ln\left(\frac{P_{\mathrm{max}}}{P_{\mathrm{min}}}\right) \ln\left(\frac{R_{\mathrm{max}}}{R_{\mathrm{min}}}\right). \tag{2.1}$$

Another way of expressing this occurrence rate is stochastically [61, 122, 121, 123, e.g.]. The number of planets within one nat of 1 $R_\oplus$ and 365 days around k stars is a Poisson random variable with rate parameter λ equal to $\Gamma_\oplus$; that is, $N \sim \mathrm{Poisson}(\lambda, k)$. For example, plugging in values from ref. [96] results in stars having zero Earth twins over four fifths of the time, and almost never more than one.

The general method is to derive probability density functions from measurements of R_p and P within some sample, and extrapolate the joint probability density to a bin covering Earth values. Fits are usually based on either (possibly piecewise) power-law priors [19, 96, 38, 125, 70], or more recently, on minimalist assumptions about the prior distribution [45, 61]. Either approach is naturally risky because the sample is noisy and incomplete [45]. Table 2–1 summarizes the various extrapolation attempts. As we see, different statistical approaches do not converge at even an accepted order of magnitude for $\Gamma_\oplus$: the true Earth twin occurrence remains poorly constrained.

No bona fide Earth twins have been detected. The G-dwarf habitable zone is nearly dead to our instruments, but we will expose it yet.

2.2 Detecting Earth twins

There is only one way to see atmospheres of habitable planets around solar-mass stars. It spatially separates planet-light from starlight; it is called direct imaging. For direct imaging in reflected light, the signal from the planet is its flux contrast, ε, with respect to the star. This is proportional to its radius and semi-major axis [126]:

$$\varepsilon \propto \left(\frac{R_p}{a}\right)^2 . \tag{2.2}$$

For an Earth twin, this signal has order 10^{-10}; i.e., one part in ten billion. Thus we appreciate that this measurement is quite delicate. However, as I allude to throughout this section, other types of signals are less optimal.

2.2.1 Probing parameter space

Where the signal from direct imaging depends on radius and semi-major axis, other detection methods return different parameters. We can combine techniques intelligently to gather more properties of a given planet, for each technique has its characteristic pros and cons [3]. The most obvious way to constrain the bulk density of a planet—as I have noted, e.g.—would be to use both the transit and radial velocity methods and measure radius and mass respectively. Only radii are known for most of the *Kepler* transiting-planet sample.

Refining planet demographics would thrive on density constraints for sub-giants [88]. No single detection method is capable of measuring mass and radius simultaneously, with the possible exceptions of transit timing variations, which can constrain masses for compact, multi-planet transiting systems [2], and transmission spectroscopy during transits (a technique discussed in section 2.3.1), which might constrain masses of Earth twins via gravitational effects on scale height [36], while others disagree [6].

As another example, direct imaging measures semi-major axis, and radial velocity measures period. Lannier et al. [76] use synthetic planets to show that combining direct imaging and radial velocity can constrain occurrence rates more accurately.

Either way, neither the transit nor the radial velocity method is particularly good at detecting Earth twins. Planets in the habitable zone of Sun-like stars are likely to transit 0.9% of the time—so this method is almost a non-starter—and current radial velocity precision ($\sim$0.8 ms^{-1}) is too poor for Earth-mass measurements (signal of $\sim$0.09 ms^{-1}) [42]. Radial velocity precision will certainly improve; the EarthFinder mission concept could constrain the masses of $\sim M_\oplus$ planets to within 10%, for example [97].

A final synergy example is the orbital fitting of directly imaged planets. This practice has already benefited from follow-up with astrometry, as opposed to additional direct imaging [99, 98]. Astrometry is a rising technique to probe Earth twin parameter space in the future [115], like direct imaging, and it is inherently good at measuring three-dimensional orbits [119].

2.2.2 Direct imaging in the next generation

Stellar photons hit a planet, are scattered by its atmosphere, and a preciously tiny fraction is reflected in our direction. This prompts the direct imaging of exoplanets. Stars are 1–10 billion times brighter than Earth twins, so we occult the starlight with an instrument either internal (coronagraph, interferometer) or, in theory, external (starshade) to the telescope.

This decade, pioneering instruments like GPI [82] and SPHERE [128] have succeeded in directly imaging giant planets at large separations (>5–10 AU) from their stars. This first-generation sample has been imaged in the infrared, capturing thermal emission rather than reflected visible light from young, hot planets. These first wide-orbit giants lit up a different demographic dark zone [16] than the habitable one [75], but the theme builds that direct imaging is good at shedding light on once-inaccessible parameter spaces [76].

As for the decades to come, several space mission concepts hinge on direct imaging. WFIRST, in the 2-m class, hopes to fly the first high-performance coronagraph in space [102]. It would have a raw contrast of 10^{-9}, allowing for the detection of reflected light from sub-Neptunes and some super-Earths. Its coronagraph inner working angle would be tight enough to reveal the habitable zones of the nearest handful of Sun-like stars.

LUVOIR and HabEx are competing concepts contending for the flagship space mission of choice in NASA's 2020 Decadal Survey. HabEx is specifically cast as a direct imaging mission targeting *Earth-size* planets [53]. This 4-m class design investigates both a coronagraph and an external starshade, and will be equipped for spectroscopic characterization possibly in both the visible and near-infrared. LUVOIR, meanwhile, exhibits a very large 10- or 15-m class architecture, explores a coronagraph design, and promises to extend from 200 nm in the ultraviolet to 2.5 μm in the infrared [111]. Characterizing habitable planets is among its many majestic science goals. The ideal raw contrast (10^{-10}) of either mission concept could resolve reflected light from Earth twins.

Needless to say, there is significant work to be done on executing the stated measurements. Beyond the severe technological challenges, the interpretation of this measurement also seems grim: albedo is unconstrained for these targets. Direct imaging does not tell us an exoplanet's geometric albedo; that is, the fraction of light backscattered towards us at full phase. To get around this, we can be less incorrect using apparent albedo A^*, defined as the ratio of the flux from the planet divided by the flux the planet would have if it were a perfectly reflecting ($A_g = 1$) Lambertian sphere at the same phase [28]:

$$A^* = \frac{(A_g = 1)\,\phi(\alpha)}{\phi_L(\alpha)}, \tag{2.3}$$

where $\phi_L(\alpha)$ is the Lambertian phase function, $\phi(\alpha)$ is the planet's true phase function, and A_g is the planet's true geometric albedo. Yet $\phi(\alpha)$ is also unmeasurable [20, 85], so we are still left making wild *a priori* estimates of A^*.

After contrast ratio, the other observable from directly-imaged planets is the projected sky-plane separation, a_{proj}, between the planet and the star. It depends on the semi-major axis as well as the orbital inclination, $i \in [0, \pi/2]$, and the orbital phase (i.e., true anomaly), $\xi \in [0, 2\pi]$. If we have enough images of the same planet at different epochs, we can constrain orbits to break this degeneracy. The actual angular separation also depends on distance r to the system, $\theta = a_{\mathrm{proj}}/r$. An Earth twin 20 pc away, if observed at maximum separation (quadrature), would show a separation on the order of 10 mas.

Direct imaging observations usually have an uneven sampling rate spanning only a fraction of the total orbit [54], so orbital fitting is suited to Markov Chain Monte Carlo methods [11, 90, 43]. Best fits come from infinite observations, of course, although the marginal usefulness of additional direct imaging epochs is not yet clear, and neither is their optimal cadence. Lannier et al. [76] demonstrate a statistical orbit-fitting tool that results in three epochs having the highest marginal accuracy increase on fits, for synthetic giant planets on wide orbits.

2.2.3 Previous estimations of Earth twin yields

LUVOIR and HabEx are designed to find Earth twins, and the accumulating evidence suggests such planets are fairly common. Yet a successful mission must also be technologically capable of this task, taking into account the physical limits on detection.

A sole group [122, 121, 123] models this situation. They predict the number of Earth twins that would be detected by direct imaging missions: $N{\sim}0$–50 over one year, under varying astrophysical and mission parameters. The method, dubbed Altruistic Yield Optimization, prioritizes target stars dynamically via calculated exposure times, and models detection probability using a binomial distribution.

One major issue with this work is the assumption that all planets are assigned $R_p = 1\,R_\oplus$. Direct imaging is biased towards larger planets, and I will show later that super-Earths and sub-Neptunes serve as planetary false positives for Earth twins. Radii are in fact constrained very poorly with real images.

Another issue with Stark et al. [122] in particular is that it assumes a conveniently-short imaging wavelength of 400 nm. Short wavelengths mean smaller inner working angles, meaning less close-in planets are obscured. However, these planets are useless if they are not also characterizable in the near-infrared, wherein lie key water vapour features. The next section discusses the characterization of the planets we detect.

2.3 Characterizing Earth twins

LUVOIR and its predecessors will have yielded us alien pale blue dots; the next step is to characterize them. By characterize, I mean every property beyond radius, mass, and orbit [37]—determining the major chemical compositions of atmospheres, inferring pressure-temperature states, or estimating heat circulation efficiencies, e.g.

2.3.1 Remote sensing

Transit spectroscopy. The road to exoplanet characterization has begun with spectroscopy. Thus far, disk-integrated measurements of starlight absorbed in *transiting* exoplanet atmospheres have been the only way to constrain the chemical compositions of these atmospheres [9]. As a planet crosses in front of its host star in the plane of the observer, the star's light curve is modified in two ways: the opaque body of the planet blocks a fraction of this light, while a smaller fraction grazes through the atmosphere and is occulted by any radiatively-active gases (so we measure the transmitted light).

The signal for a given spectral feature is the total count of photons received, N_{tot}, times the fraction of photons intercepted by the atmosphere, f_p. These terms are parameterized as

$$N_{\text{tot}} = \frac{\pi^2 \tau \Delta t}{hc} \left(\frac{R_* D}{2r} \right)^2 \int_{\lambda_1}^{\lambda_2} B(\lambda, T_*) \lambda \mathrm{d}\lambda, \tag{2.4}$$

where τ is the system throughput (the ratio of photons incident on the telescope focal surface to photons incident on the primary mirror), Δt is the integration time, R_* is the stellar radius, $\lambda_1 - \lambda_2$ is the bandpass, r is the distance to the star, D is the telescope diameter, T_* is the stellar effective temperature, and $B(\lambda, T_*)$ is the Planck function [31]; and

$$f_p(\lambda) = \frac{2 R_p h(\lambda)}{R_*^2} \tag{2.5}$$

where $h(\lambda)$ is the altitude below which the atmosphere can be considered effectively opaque, about 10 km for Earths [63]. This quantity f_p represents the fraction of the stellar disk area covered by the absorbing part of the planetary atmosphere. For an Earth twin at 20 pc, f_p has order 10^{-7}, and the signal is <1 count per hour-long exposure. Transit methods have poor signals, poor signal-to-noise ratio, and unworkable observation windows.

The best targets for transmission spectroscopy are those planets whose atmospheres have large scale heights (e.g., H_2 atmospheres), and whose radii are large relative to the radius of their host star. Super-Earths are the smallest planets whose atmospheres are still detectable in transit by JWST, and their characterization is an expected result of this mission [5, 9, 88]. Current telescopes can only measure giant planet spectra with good precision; so far, water vapour absorption has been detected in a handful of hot Jupiters and a warm Neptune [46]. Detections in smaller planets remain contested [27].

Imaging spectroscopy. As mentioned previously, exoplanets in the habitable zone of Sun-like stars are very unlikely to eclipse their star, so transit spectroscopy is not a reliable way to characterize their atmospheres. The alternative is simply the spectroscopic analog of direct imaging photometry.

Currently, imaging spectroscopy is conducted at the ground-based telescopes outfitted with extreme coronagraphic instruments and using adaptive optics, such as the Gemini Planet Imager at the Gemini telescope and SPHERE at the Very Large Telescope. These instruments are capable of detecting features in the atmospheres of giant planets and brown dwarfs, highlighting their inter-group diversity [12].

Before we tackle smaller planets, WFIRST aims to measure spectra of gas giants. Radius and illumination phase angle are degenerate, however, so it remains to show how these results will be meaningful [89]. In theory, spectroscopy could put constraints on radius if the reflectance in certain wavelength regimes is independent of albedo [85].

Observations of Earthshine are an interesting contrivance for modeling the Earth twin spectra of our dreams [133]. Earthshine refers to the reflection of Earth-light off the night side of the moon. In this way, we can look at the real

Earth as if it were an unresolved exoplanet. The spatial unmixing of cloud, ocean, and vegetation cover fractions has been demonstrated, as have detections of biosignature gases [87].

2.3.2 Colours

A “compromise” between spectroscopy and single-band photometry is looking at the colours of planets; that is, ratios of one photometric band’s intensity to another. Groups of exoplanets with similar surface or atmospheric properties could occupy characteristic locations in colour-colour diagrams; i.e., plots of two ratios comprising three or four bands [124]. A Mars twin’s rocky surface and thin atmosphere will make it brighter in the red, in the solar system example, while methane deep in a Neptune twin’s atmosphere will absorb in the red, making it brighter in the blue-green [126]. And famously, Rayleigh scattering in Earth’s atmosphere renders us blue.

Crow et al. [32] showed colours can identify Earth among the solar system planets and Titan, based on observations from the EPOXI mission. Using modeled spectra, colours have picked out Cenozoic Earth from more exotic worlds [73], but only under the assumption of cloud-free atmospheres. Mayorga [85] showed how colour analysis is complicated further by the effects of stellar illumination phase angle, which convolute this more strongly than models had predicted.

2.3.3 Exo-cartography

The Earth system is clearly tied to the distribution of its continents and oceans. Especially so, coexisting water and land reinforces our long-term habitability. Planets without this mix may not have a significant silicate weathering feedback, which regulates the CO_2 greenhouse on Earth and keeps our climate temperate [27].

With exo-cartography, we can infer the number, reflectance spectra, and longitudinal locations of major surface types [40, 49, 67, 29]. This works because directly-imaged planets show diurnal brightness variations as different surface and cloud features rotate into view [30]. The lightcurve collected from the planet is the disk-integrated reflectance per exposure. In theory, we can invert lightcurves to piece out latitude-longitude albedo maps [66].

Where spectroscopy gives us the reflectance per wavelength (with no spatial information), exo-cartography would give us the reflectance per spatial coordinate (with only broadband spectral information, or colours). We wait patiently for our descendants to build a kilometers-wide telescope in space which could spatially resolve Earth twins and acquire spectra at each pixel.

Year	Ref.	$\eta_\oplus$	$\Gamma_\oplus$	R_p ($R_\oplus$)	P (days)	Method	Notes
2011	Catanzarite & Shao [23]	$0.011^{+0.006}_{-0.003}$	$0.022^\dagger$	[0.8, 2]	[338, 585]	power law fit	small, fiducally complete sample of $P < 132$ days and $R > 2\ R_\oplus$
2011	Youdin [135]	-	$2.75^{+0.33}_{-0.33}$	-	-	ML, power law	small sample of $P < 50$ days
2012	Traub [125]	$0.34^{+0.14}_{-0.14}$	$0.16^\dagger$	[0.5, 2.0]	[223, 1032]	power law fit	small sample of $P < 42$ days, FGK stars
2013	Dong & Zhu [38]	0.28	$0.070^\dagger$	[1, 2]	[0.75, 250]	ML, power law	flat dist. for $P > 10$ days, but insecure for $P > 50$ days., solar metallicities
2013	Fressin et al. [47]	$0.0165^{+3.6}_{-3.6}$	$0.00832^{\dagger,a}$	[0.8, 1.25]	<85	IDEM	FGK stars, short periods only
2013	Petigura et al. [96]	$0.057^{+1.7}_{-2.2}$	$0.12^\dagger$	[1, 2]	[200, 400]	IDEM, power law	GK stars
2014	Foreman-Mackey, Hogg, & Morton [45]	-	$0.019^{+0.010}_{-0.008}$	-	-	HBM	G dwarfs
2015	Christiansen et al. [26]	$0.0729^{+2.31}_{-2.31}$	$0.152^\dagger$	[1, 2]	[160, 320]	IDEM	FGK stars
2015	Burke et al. [19]	0.1	$0.6^\dagger$	[0.8, 1.2]	[292, 438]	ML, power law	GK dwarfs
2015	Silburt, Gaidos, & Wu [118]	$0.064^{+3.4}_{-1.1}$	$0.11^\dagger$	[1, 2]	[360, 809]	IS	solar twins
2018	Kopparapu et al. [70]	$0.30^{+0.74}_{-0.21}$	$0.45^\dagger$	[0.5, 1]	[365, 948]	occurrence model from SAG13 meta-analysis	solar twins
2018	Hsu et al. [61]	$0.41^{+0.29}_{-0.12}$	$1.6^{+1.2}_{-0.5}$	[1.0, 1.5]	[237, 320]	HBM, ABC, SIS	FGK stars

Table 2–1: Occurrence rates, $\eta_\oplus$, and corresponding rate densities, $\Gamma_\oplus$, for Earth-size planets in the habitable zones of Sun-like stars.

Statistical methods are abbreviated as: ML, Maximum Likelihood; IDEM, Inverse Detection Efficiency Method; HBM, Hierarchal Bayesian Model; IS, Iterative Simulation; ABC, Approximate Bayesian Computing; SIS, Sequential Importance Sampling. †Where values of $\Gamma_\oplus$ are not reported in the original paper, I calculate them here via equation 2.1, assuming constant $\eta_\oplus$ across that period and radius range. ^{a}Value is sensitive to the choice of inner period cutoff.

Chapter 3
A submitted manuscript: Quantifying biases and planetary false positives

This chapter comprises the full text of a manuscript, ref. [57], accepted for publication in the Astronomical Journal on March 30, 2018.

3.1 Abstract

Direct imaging is likely the best way to characterize the atmospheres of Earth-sized exoplanets in the habitable zone of Sun-like stars. Previously, Stark et al. [122, 121, 123] estimated the Earth twin yield of future direct imaging missions, such as LUVOIR and HabEx. We take an important next step by extending this analysis to other types of planets, which will act as false positives for Earth twins. We define an Earth twin as any exoplanet within half an e-folding of 1 AU in semi-major axis and 1 $R_{\oplus}$ in planetary radius, orbiting a G dwarf. Using Monte Carlo analyses, we quantify the biases and planetary false positive rates of Earth searches. That is, given a pale dot at the correct projected separation and brightness to be a candidate Earth, what are the odds that it is, in fact, an Earth twin? Our notional telescope has a diameter of 10 m, an inner working angle of $3\lambda/D$, and an outer working angle of $10\lambda/D$ (62 mas and 206 mas at 1.0 μm). With no precursor knowledge and one visit per star, we detect many more un-Earths—77% of detected candidate Earths have an un-Earthlike radius and/or semi-major axis, and their mean radius is 2.3 $R_{\oplus}$, a sub-Neptune. The odds

improve if we image every planet at its optimal orbital phase, either by relying on precursor knowledge, or by performing multi-epoch direct imaging. 47% of detected Earth twin candidates are false positives in this targeted scenario, with a mean radius of 1.7 $R_{\oplus}$. The false positive rate is robust to stellar spectral type and the assumption of circular orbits.

3.2 Introduction

Planned direct imaging missions would measure the reflectance spectra [83] and photometric variability [44] of Earth-sized planets orbiting in the habitable zone of nearby Sun-like stars. Many studies have shown that direct imaging is also a viable way to discover these planets [1, 123, 121, 122]. Given enough time, a mission could discover hundreds to thousands of planets and characterize them all. In practice, there will only be enough time to characterize some of these worlds in detail. We would therefore like to distinguish between Earths and un-Earths as efficiently as possible. For although they are expected to revolutionize many aspects of planetary science, mission concepts such as LUVOIR and HabEx are being motivated based on their ability to characterize Earth twins.

Brown [17] presented a "photometric and obscurational single-visit completeness" method to estimate the chance, for a particular star, that a companion exoplanet is detectable during one visit given that the planet exists. In their model, "photometric" refers to the condition that the planet/star contrast must exceed the inherent instrument floor in photon counting. "Obscurational" refers to how the planet and its star must be positioned in the sky plane, such that the planet is outside the inner obscuring disk of the coronagraph or starshade. This inner working angle (IWA) is defined technically as the angle at which transmission decreases by 50%. Coronagraphs may also have an outer working angle (OWA), beyond which starlight is no longer adequately suppressed. Obscuration and low contrast are the two dominant factors that could hinder a detection.[1]

If one is equally interested in all planets, then an "average" mission completeness suffices, without looking at the demographics of the mission's yield. But what if one prefers a certain kind of planet? Then we would do best to consider how a mission may be biased towards inopportune radii and semi-major axes.

While Stark et al. [122, 121, 123] cared about semi-major axes between 0.7–1.5 AU, they assigned a radius of 1 $R_\oplus$ to all planets in their completeness calculator. In reality, most planets are not the size of Earth.

And the crux: any mission capable of finding Earth twins will have an easier time finding other sorts of planets. Hence, we want to not only detect as many Earth twins as possible, but also know that a detected planet is an Earth twin. Many un-Earths will show up at the correct projected separation and brightness to be Earthlike. We would confuse these planets with true Earth twins, so we call them false positives.

---

[1] Others include exo-zodiacal dust [103] and integration time.

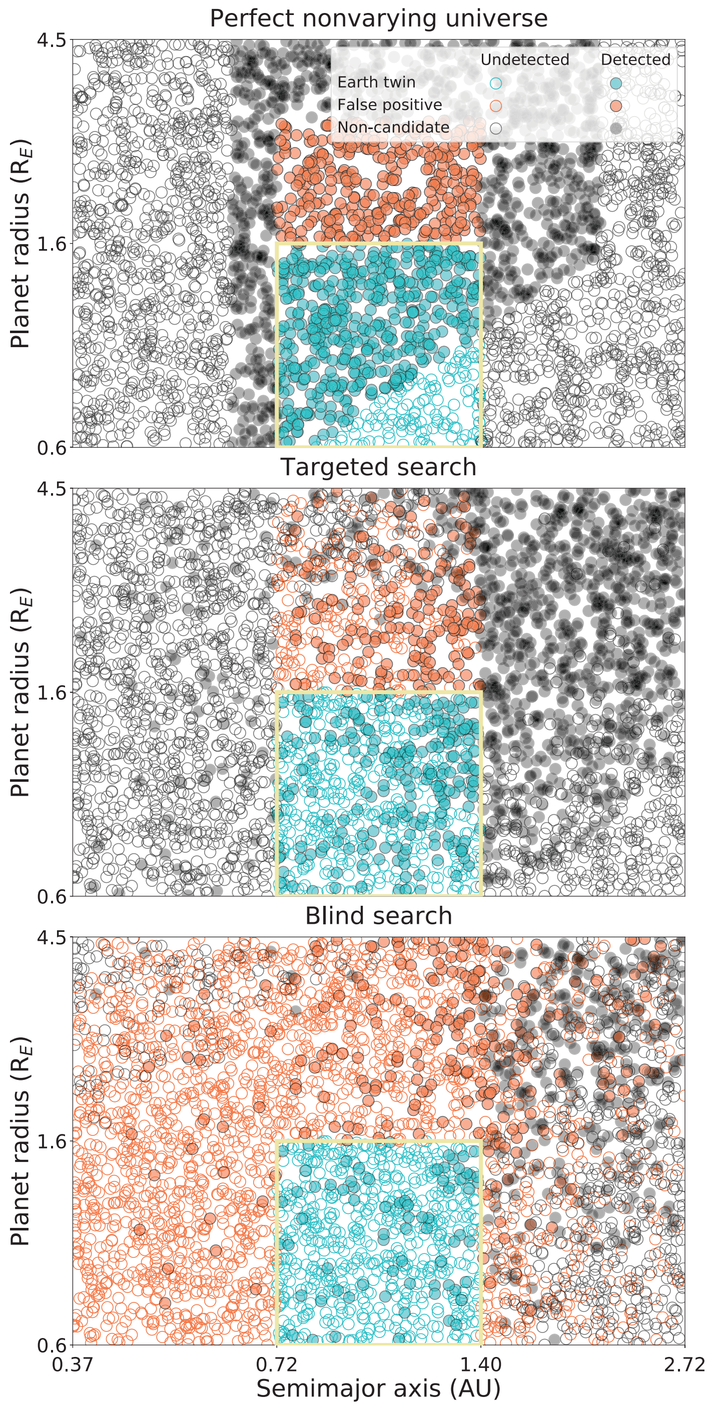
Perfect nonvarying universe
Undetected
Detected
Earth twin
False positive
Non-candidate
4.5
1.6
0.6
Planet radius (R$_E$)
Targeted search
4.5
1.6
0.6
Planet radius (R$_E$)
Blind search
4.5
1.6
0.6
Planet radius (R$_E$)
0.37
0.72
1.40
2.72
Semimajor axis (AU)

Figure 3–1:

Figure 3–1 *(opposite)*: Demographics of detected (filled) and undetected (hollow) planets for three simulated surveys. Blue denotes an Earth twin, while orange denotes a false positive, and grey denotes a planet that would not be mistaken for an Earth twin. *Top*: a survey of an ideal universe with every star at 10 pc, and planets with face-on inclination and 30% albedo. *Middle*: a search of a universe where stellar distance and orbital inclination vary randomly; albedo can uniformly vary from 0.05 to 0.5, and the planet is imaged at gibbous phase just outside the inner working angle. *Bottom*: a search of a universe where distance, inclination, albedo, and orbital phase are random. The grid cell defining Earth twins is highlighted in yellow. Planets are distributed log-uniformly in semi-major axis and radius. Based on a simulation with stellar number density inflated by $\sim$1.5 orders of magnitude to 5×10^3 stars, for visualization.

3.2.1 An observation flowchart

Suppose we image a star and see a dot that we have identified as a companion, and which may be a newly-discovered Earth twin. Our options include: (i) we get a spectrum of the dot immediately; or (ii) we return to this star at a later epoch, to better constrain the companion's semi-major axis, hoping that the planet has not become obscured by the IWA or confused with another planet in the system. If we choose option (ii), and the next image is not dissuading, then the choices are the same, *ad infinitum* until we are ready to commit to spectroscopy.[2] A third option is to get another image in a different filter, if one believes that colour is a useful discriminant between different types of planets [73], but phase-variable colours make this strategy more challenging [22, 85].

Roughly speaking, one direct imaging detection provides two data: the RA and Dec of the planet relative to its host star. There are seven orbital parameters, so $\gtrsim$4 detections are needed to establish an orbit. However, it is beyond our current scope to determine the best number of revisits, or their cadences.

Rather, our analysis considers two endmember scenarios. In "blind" searches, we assume no prior observations of the planet; our only known parameters are the two first-order direct imaging observables of planet/star brightness contrast, ε, and projected separation, $a_{\rm proj}$.

[2] A silver lining to obtaining spectra of un-Earths is that they provide a control for biosignatures, as long as we eventually determine which planets are in fact habitable.

On the other hand, in "targeted" searches, we have the luxury of knowing where and when to look at each system. We assume their orbits can be predicted, based on data from either multi-epoch direct imaging, radial velocity,[3] or astrometry. The Keplerian orbital fits from these observations are adequate for us to target the wanderers at gibbous phase outside the IWA [116, 21, 99].

We therefore investigate how well a direct imaging mission can distinguish between Earths and un-Earths, based solely on photometry. Particularly, we focus on the "blind" and "targeted" observation scenarios. In section 3.3, we describe our Monte Carlo method for simulating exoplanets and evaluating their detectabilities. Section 3.4 presents results, and section 3.5 our discussion, including a sensitivity analysis to test our assumptions.

3.3 Modeling methodology

3.3.1 Direct imaging signal scaling

The signal from a directly imaged planet is the planet/star contrast ratio, parameterized for reflected light as

$$\varepsilon = A^* \, \phi_L(\alpha) \left(\frac{R}{a}\right)^2, \tag{3.1}$$

with planetary radius R, semi-major axis a, and apparent albedo A^* [126]. The phase function $\phi_L(\alpha)$ describes how the light scattered by a planetary atmosphere changes with the star-planet-observer angle α. For the purposes of our numerical

[3] Radial velocity leaves two orbital parameters unconstrained: orbital inclination and longitude of the ascending node.

experiment, we adopt the Lambertian phase function:

$$\phi_L(\alpha) = \frac{1}{\pi}\left[\sin\alpha + (\pi - \alpha)\cos\alpha\right]. \tag{3.2}$$

The phase angle is related trigonometrically to orbital phase ξ and inclination i [126]:

$$\alpha = \cos^{-1}\left(\cos\xi \sin i\right). \tag{3.3}$$

3.3.2 Conditions for detectability

Now for illustration—figure 3–1 illustrates the detection conditions for direct imaging. The top panel shows detected and undetected planets for an idealized survey in which all stars are at the same distance and all planets are in face-on orbits and have the same albedo. The only parameters allowed to vary here are planetary radius and semi-major axis. We see a distinct wedge-shaped pattern with sharp inner and outer working angle cutoffs (left and right, respectively), and a hard-edged contrast floor (bottom right).

Photometric condition. For a planet to be detected, its planet/star contrast ratio must exceed the coronagraph raw contrast, $\varepsilon > \varepsilon_{\min}$. We assume an optimistic LUVOIR-esque value of $\varepsilon_{\min} = 1 \times 10^{-10}$. This implicitly assumes a volume-limited survey, such that integration time per target is allotted as generously as necessary to achieve the intended signal-to-noise ratio [122].

Obscurational condition. Detectable planets must also have a projected separation a_{proj} falling outside the IWA of the coronagraph, and inside the OWA. That is, $a_{\mathrm{IWA}} < a_{\mathrm{proj}} < a_{\mathrm{OWA}}$. Both angles are set by some multiple of λ/D, where D is telescope diameter. The IWA is often not actually a hard cutoff; it denotes the angular separation where the instrument sensitivity drops to 50% its nominal value. The approximation is nonetheless reasonable [122].[4]

Projected separation is the planet's semi-major axis convolved with orbital elements,

$$a_{\text{proj}} = a\sqrt{\sin^2 \xi + \cos^2 \xi \cos^2 i}, \tag{3.4}$$

so $a_{\text{proj}} \leqslant a$. For now we assume circular orbits, but we test this assumption below.

The IWA limit is important for targets orbiting distant stars and/or at long wavelengths, while the OWA will pose a challenge for planets orbiting the nearest stars. The OWA is mostly of concern for blind surveys. If we already know a planet's orbit, then we can target it at a gibbous phase with a sufficiently small projected separation (and better contrast), unless the orbital inclination is too small.

3.3.3 Generation of planet parameters

The bottom two panels of figure 3–1 illustrate searches of realistic universes, where we draw more parameters than just R and a from probability density functions. This section describes these density functions.

Demographics: radius and semi-major axis. Petigura et al. [96] showed that near 1 $R_\oplus$ and 365 days, the phase-space density of planets is approximately uniform in its natural logarithms (the actual variation was a factor of two). This distribution easily applies to semi-major axis due to Kepler's Third Law.

[4] The sensitivity slope has a $\Delta\lambda/D$ of $\sim$1 [58], which is short compared to the OWA-IWA $\Delta\lambda/D$ difference of 7 adopted here.

We adopt log-uniform demographics but test the impact of this assumption below. The normalized probability densities are

$$\frac{\mathrm{d}f}{\mathrm{d}(\ln R)} = \frac{1}{\ln\left(R_{\max}/R_{\min}\right)} \tag{3.5}$$

and

$$\frac{\mathrm{d}f}{\mathrm{d}(\ln a)} = \frac{1}{\ln\left(a_{\max}/a_{\min}\right)}. \tag{3.6}$$

These describe the likelihood of a planet having radius R and semi-major axis a, given that the planet exists within that range of semi-major axes and radii. For a given star, the probability of a planet occurring in our playing field is about 7 in 10, as explained in section 3.3.4. Note that these ranges are broader than our adopted definition for Earth twins (see figure 3–1).

For mathematical convenience, each cell in our 3×2 a-R grid (figure 3–1) has a height of one e-folding in R and a width of $e^{2/3}$ in a (equal to one e-folding in period). The axis limits are chosen such that the cell defining Earth twins is centred at 1 AU and 1 $R_\oplus$.

Orbital elements: phase and inclination. At a given point in time, planets can be anywhere along their orbits. We assume circular orbits, so orbital phase is uniformly distributed in $\xi \in [0, 2\pi)$, and the normalized distribution function is

$$\frac{\mathrm{d}f}{\mathrm{d}\xi} = \frac{1}{2\pi}. \tag{3.7}$$

Meanwhile, inclination varies between 0 and $\pi/2$ and is uniform in $\cos i \in [0, 1]$:

$$\frac{\mathrm{d}f}{\mathrm{d}(\cos i)} = 1. \tag{3.8}$$

Inclination is an unchanging property of a planet, but orbital phase, by definition, varies as the planet orbits its star. For a given inclination and semi-major axis, there exists a maximum detectable planet/star contrast, occurring each orbit, associated with a certain orbital phase. This "optimal phase" depends on our choice of phase function model. Assuming the planet is a Lambertian reflector, the optimal phase is at the gibbous phase corresponding to $a_{\mathrm{proj}} = a_{\mathrm{IWA}}$, or simply the fullest unobscured phase.

Analytically, the phase angle α corresponding to the optimal phase is given by substituting $a_{\mathrm{proj}} = a_{\mathrm{IWA}}$ into equation 3.4, solving for ξ, and then substituting the result into equation 3.3:

$$\alpha_{\mathrm{opt}} = \sin^{-1}\left(\frac{a_{\mathrm{IWA}}}{a}\right). \tag{3.9}$$

This equation has multiple roots; we are interested in the gibbous phase, so phase angle is $\alpha_{\mathrm{opt}} \in \left[0, \frac{\pi}{2}\right]$.

Planetary albedo. The distribution of planetary albedos is completely unconstrained for exoplanets at large separations. We parameterize this uncertainty by allowing A^* to vary over an order of magnitude, with uniform probability:

$$\frac{\mathrm{d}f}{\mathrm{d}A^*} = \frac{1}{A^*_{\max} - A^*_{\min}}. \tag{3.10}$$

We have adopted conservative values of $A^*_{\max} = 0.5$ and $A^*_{\min} = 0.05$. As we will show in section 3.5.1, the false positive rate in a blind search is insensitive to the underlying albedo distribution, or our knowledge thereof. Shrinking the albedo range decreases the false positive rate in targeted searches, but only under certain assumptions.

Distance to system. We assume a constant density of stars out to the farthest distance probed $r_{\max}$, so the likelihood of a planetary system falling within a sphere of radius r is proportional to r^2. The normalized probability density is therefore

$$\frac{\mathrm{d}f}{\mathrm{d}r} = \frac{3}{r_{\max}^3} r^2. \tag{3.11}$$

Unfavourable orbits and/or greater distances shorten the time a planet spends between the inner and outer working angles. This decreases the number of detections, compared to a nonvarying universe (cf. top and bottom panels of figure 3–1). The difference between figure 3–1's middle and bottom panels is due to the planet's location in its orbit, ξ, at the time of the image. In the middle panel, we assume that the orbit of each planet is known, so we know to target stars when the planet is brightest and unobscured. On the other hand, blindly searching stars for planets is equivalent to drawing ξ from its density function (eq. 3.7), as in the bottom panel.

3.3.4 Mission parameter assumptions

Telescope diameter. Our notional telescope has a 10-m primary mirror, comparable to the proposed architecture B of LUVOIR and slightly greater than architecture A of HabEx.

Wavelength. We use a wavelength of 1.0 μm to image planets in reflected starlight. This is consistent with Stark et al. [121]; they choose 1 μm as their baseline characterization wavelength due to the water vapour feature at 0.95 μm. Although searching at 0.4 μm would yield more Earth twins because the IWA would be smaller, merely finding planets at this shorter wavelength is fruitless if we cannot also characterize them.

Working angles. We adopt an IWA of $3\lambda/D$ and an OWA of $10\lambda/D$, similar to the "pessimistic" case of Stark et al. [121].

Contrast. We assume the coronagraph has a raw contrast of $\varepsilon_{\min} = 1 \times 10^{-10}$. This threshold is often quoted as the technological goal for detection of Earth-sized planets [39, 100, 35]. We further assume that post-processing would provide an extra order of magnitude in contrast, enabling robust detection of planets at $\varepsilon_{\min}$.

Maximum survey distance. Since we have adopted a fairly long wavelength with an accordingly large IWA, the distances at which we can probe Earth twins are limited. Larger distances drive $a_{\rm IWA}$ outwards. An Earth twin $r_{\max}$ parsecs away, orbiting at $a_{\oplus,\max}$, would just reach the IWA at maximum elongation; any stars beyond this point could not host *detectable* Earth twins. This sets our maximum survey distance:

$$r_{\max} = \frac{a_{\oplus,\max}}{\rm IWA} = 22.6 \text{ pc}. \tag{3.12}$$

This is a much smaller search volume than Stark et al. [122, 121], who choose the round number of 50 pc as their maximum distance using telescope diameters of 4–20 m.

Number of targets. We assume that our survey is volume-limited, and that stars are evenly distributed across the search volume. This lets us quickly calculate the number of target stars within a sphere defined by our maximum survey distance. We use the stellar density model from Bovy [15]:

$$\frac{\mathrm{d}N_*}{\mathrm{d}V\mathrm{d}M_*} = (0.016\ \mathrm{pc}^{-3}\ M_\odot^{-1})\ \left(\frac{M_*}{M_\odot}\right)^{-4.7}, \tag{3.13}$$

which we integrate over [0.84, 1.15] $M_\odot$.

In reality, not only are ∼50% of Sun-like stars in binary pairs [8], but the period distribution of binaries peaks at 10,000 days [74], about the semi-major axis of Saturn. These companion stars may pose a problem for starlight suppression. Although one could improve detection yields by a factor of ∼2 with careful attention to coronagraph design, this is outside the scope of our current paper. We therefore eliminate half the target stars; the number of target stars in a given simulated survey is:

$$N_* = \texttt{floor}\left(\frac{1.793 \times 10^{-2}\ r_{\mathrm{max}}^3}{2}\right). \tag{3.14}$$

This evaluates to 136 G-type stars for $r_{\mathrm{max}} = 22.6$ pc. For comparison, Stark et al. [122] report a target list of 5449 stars within 50 pc and with spectral type A to M. Substituting these limits—excepting M-dwarfs[5] —into equation 3.13, we get 4937 stars.

Simulating a realistic target list, however, is not the focus of this work. We report absolute numbers primarily as a sanity check. Indeed, most of our figures and statistics come from running 100 simulated surveys to minimize Poisson noise. Results are otherwise unaffected by our chosen N_*.

[5] Only one M-dwarf, Proxima Centauri, is near enough to host Earth twins outside our adopted IWA.

To populate each star with 0 or more planets with radius $R \in [R_{\min}, R_{\max}]$ and semi-major axis $a \in [a_{\min}, a_{\max}]$, we assume an across-the-board occurrence rate density of $\Gamma = \mathrm{d}N_p/(\mathrm{d}\ln R\,\mathrm{d}\ln P) = 0.12$ planets per star per per natural logarithmic bin in period and radius [96, 70]. This corresponds to an occurrence rate, η, of 0.7 planets per star. In accordance with Poisson statistics, most stars have 0, 1, or 2 planets.

3.4 Results

We define Earth twins in terms of planetary radius and semi-major axis. A planet orbiting a G-dwarf with $R \in \left[e^{-1/2}, e^{1/2}\right] R_\oplus$ and $a \in \left[e^{-1/2}, e^{1/2}\right]$ AU is an Earth twin. Note that both ranges correspond to one e-folding; e.g., $R_{\oplus,\max} = eR_{\oplus,\min}$. This is convenient because planetary demographics are often reported as $\mathrm{d}N/(\mathrm{dln}R\ \mathrm{dln}P)$, so the Earth twin rate is simply equal to the rate density at Earth. Our Earth twins roughly encompass the "rocky" and "super-Earth" classes of Kopparapu et al. [70], who classify planets based on expected atmospheric chemistry. Of course, there is no evidence that all planets with the same size and orbit as Earth are anything like Earth.

3.4.1 Planetary false positive rates

Locating Earth twins in figure 3–1 is easy—they all live in the highlighted centre grid cell on the bottom row. The problem is that a single epoch of direct imaging does not yield semi-major axis and radius, but rather, projected separation and contrast ratio. Locating Earth twins on *those* axes is much trickier. We must sift through some number of un-Earthlike planets, indistinguishable from our real quarry.

We now calculate the likelihood that a planet actually is an Earth twin, given that it is detected in the contrast-separation region where an Earth twin could appear. We label this region the Earth twin candidate zone; it denotes where an Earth twin might conceivably show up in a direct imaging snapshot. The extent of the candidate zone depends on whether or not we know the planets' orbits.

Candidates in blind searches. If we know nothing about orbital phase or inclination, then the projected separation of an Earth twin on a circular orbit is at most $a_{\oplus,\max}$, and can be as small as 0: $0 \leqslant a_{\text{proj}} \leqslant a_{\oplus,\max}$. The maximum planet/star contrast for an Earth twin is $\varepsilon_{\max} = (R_{\oplus,\max}/a_{\oplus,\min})^2$; this comes from setting the apparent albedo to unity, adopting the largest Earthlike radius, and adopting the largest possible value of $\phi_L/a^2 \approx 1.44/(\pi a_{\text{proj}}^2)$.[6] An Earth twin with $a_{\text{proj}} = 0$ and/or $\varepsilon < \varepsilon_{\min}$ is not detectable at that epoch, but a non-detectable Earth twin is still relevant.

Candidates in targeted searches. If we know the orbital phase and inclination, then a can be calculated from a_{proj} (eq. 3.4), and the semi-major axis criterion for Earth twin candidacy is $a_{\oplus,\min} \leqslant a \leqslant a_{\oplus,\max}$.

To get the maximum contrast ratio, we divide ε by its Lambertian phase function, again setting A^* to unity, to compare against the stricter limit

$$\varepsilon' \leqslant \left(\frac{R_{\oplus,\max}}{a}\right)^2 \tag{3.15}$$

[6] Given an observed projected separation, there is a trade-off between the semi-major axis (smaller a are brighter) and orbital phase (smaller α are brighter). One can numerically solve for the maximum contrast ratio, which occurs at an orbital phase of about 63 degrees.

where ε' is the phase-standardized contrast.

Un-Earthlike planets falling within the Earth twin candidate zone are false positives. They appear there for one or more of the following reasons:

1. $a < a_{\oplus,\mathrm{min}}$, but due to the planet's unknown phase and inclination, we cannot rule it out as an Earth twin in gibbous or crescent phase.
2. $a > a_{\oplus,\mathrm{max}}$, but the planet is in gibbous or crescent phase, so its projected separation appears smaller.
3. $R > R_{\oplus,\mathrm{max}}$, but the planet has low albedo, decreasing its planet/star contrast to something reasonable for an Earth twin.

The degeneracy between projected separation and semi-major axis can be broken if a planet is imaged at a known orbital phase, hence ruling out the first two scenarios and ameliorating the third.

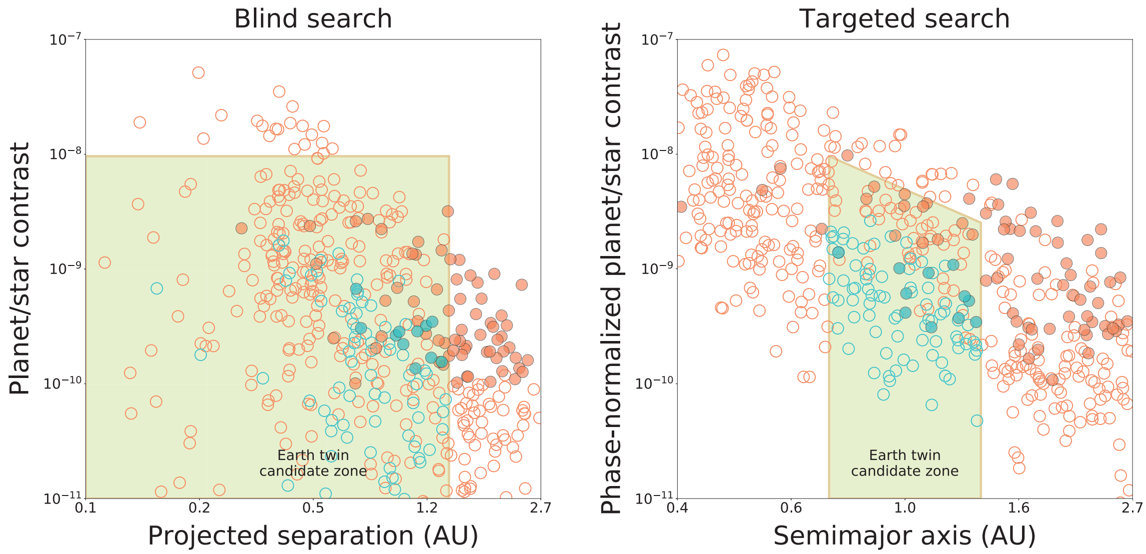

Figure 3–2: A comparison of survey returns in terms of the direct imaging observables, for a blind survey where planets are at random orbital phase (left), versus a survey revisiting known planets at their brightest observable phase (right). Based on a simulated survey with 10^3 stars; i.e., inflated by an order of magnitude, for visualization. Yellow regions show the “candidate zone” where a true Earth twin could possibly fall. Solid circles are detected planets, while empty circles are undetected planets. Blue circles represent Earth twins, and orange circles are un-Earths. Orange filled circles within the shaded region constitute planetary false positives: un-Earths masquerading as Earth twins.

Quantifying the false positive rate. We essentially count the filled dots (the detected planets) in figure 3–2 to find the false positive rate of a survey:

$$\mathrm{FPR} = \frac{[\#\text{ un-Earths}]_{\mathrm{det,ETCZ}}}{[\#\text{ un-Earths}]_{\mathrm{det,ETCZ}} + [\#\text{ Earths}]_{\mathrm{det}}}, \tag{3.16}$$

where the subscript ETCZ refers to a planet falling in the Earth twin candidate zone.

Similarly, the fraction of Earth twins detected is the number of filled teal dots to the number of teal dots:

$$f_{\mathrm{det},\oplus} = \frac{[\#\ \mathrm{Earths}]_{\mathrm{det}}}{[\#\ \mathrm{Earths}]_{\mathrm{total}}}, \tag{3.17}$$

which we call the detection efficiency of the survey. This metric, like the false positive rate, describes the survey as a whole (cf. completeness from Brown [17] being a function of a star). It is strongly dependent on the size of the search volume: visiting more distant stars becomes less efficient, despite the higher cumulative yield of planets (figure 3–3).

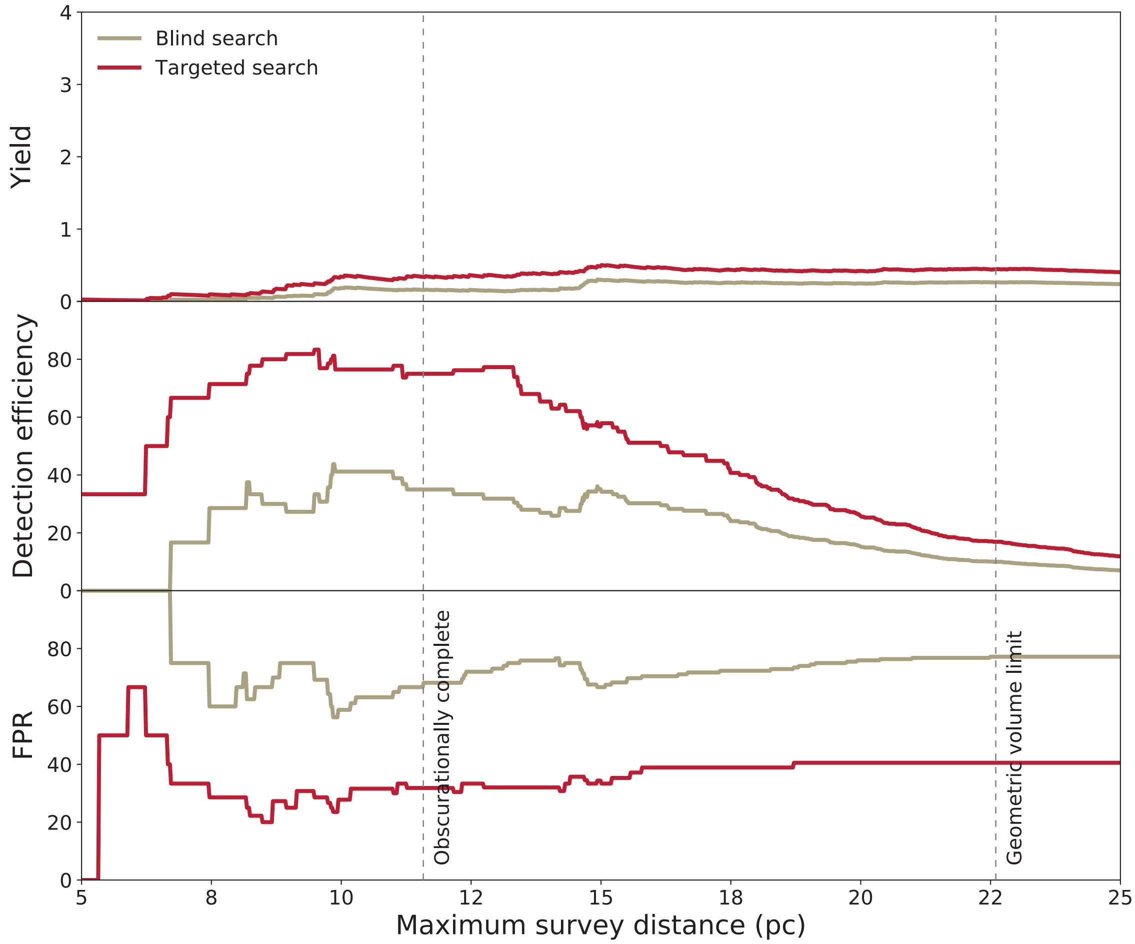

Figure 3–3: Search volume dependence of cumulative Earth twin yield (top), cumulative Earth twin detection efficiency (middle), and cumulative false positive rate (bottom), for blind searches (grey lines) and targeted searches (red lines). Dashed vertical lines represent the distances at which a planet's projected angular separation would be just inside the IWA, if it orbited at $a_{\oplus,\min}$ ($r_{\max} = 11.6$ pc), and if it orbited at $a_{\oplus,\max}$ ($r_{\max} = 22.6$ pc). A targeted survey out to the leftmost dashed line would therefore detect every Earth twin bright enough to surpass the contrast floor, while no additional Earth twins could be detected beyond the rightmost dashed line. Calculated from 10^5 simulated stars, where yields are scaled to the realistic number of stars at the given $r_{\max}$ (equation 3.14).

Table 3–1 presents the false positive rate for blind and targeted searches. Imaging planets at their optimal orbital phases produces a lower false positive rate because the Earth twin candidate zone is smaller. Targeting planets at their optimal phases slightly improves their planet/star contrasts and minimizes the odds of missing a planet inside the IWA.

However, knowing orbits to break degeneracy is the key here, as opposed to a better-timed observation. Merely increasing the Earth twin yield via waiting for brighter and unobscured phases—without changing the candidate zone area accordingly—actually increases the false positive rate by a few percentage points to 81%. This is because more un-Earths are also detected alongside the Earth twins.

The false positive rate of a blind survey (77%) can be improved by multiple visits. Candidates are only detectable for a fifth of their orbit on average, under our mission parameters, so subsequent visits may reveal elusive planets.

Table 3–1 also reports the biases in these searches. Most detected Earth twin candidates will have radii large enough such that they must have massive gaseous envelopes, making them sub-Neptunes [81, 50, 108]. Phase knowledge reduces the mean radius of detected candidates from 2.3 $R_\oplus$ to 1.7 $R_\oplus$—just outside our Earth twin box.

The worst culprits are planets with radii too large to be Earthlike, but whose low albedos reduce their planet/star contrasts. For a blind search, we find that 67% of Earth twin candidates will fall in this category. This statistic drops to 47% for targets at known phase.

Semi-major axis degeneracy only creates false positives for a blind search. In this scenario, planets orbiting exterior to $a_{\oplus,\max}$ make up 27% of Earth twin candidates. Finally, planets interior to $a_{\oplus,\min}$ make up 9% of candidates. Note that these categories do not add to 100% because they are not all mutually exclusive.

	Blind	Targeted
False positive rate (%)	77	47
Mean Earth twin candidate R ($R_\oplus$)	2.3	1.7
Mean Earth twin candidate a (AU)	1.2	1.1

Table 3–1: False positive rates and biases in planetary radius R and semi-major axis a for a blind survey, versus a survey targeting planets with known orbits. False positive rate calculated via equation 3.16, and detection efficiency via equation 3.17. Based on 10^5 simulated stars.

As a sanity check, we can estimate Earth twin yields based on a realization scaled to a realistic number of targets, $N_* = 136$ G stars. Our simulation finds $\sim$2 Earth twins in a blind search, and $\sim$5 in a targeted search. Of course, our yields vary under different model assumptions, as we discuss throughout the rest of this paper.

To compare our yield results with Stark et al. [122], we adopt their baseline mission parameters: a less forgiving telescope diameter of 8 m and IWA of $4\lambda/D$, but a more optimistic $\lambda = 550$ nm, and a larger target list of 5449 FGK stars within 50 pc. We also follow suit by fixing the occurrence rate, $\eta_\oplus$, at 0.1 planets per star across our original a-R area. A targeted search under these assumptions finds $\sim$5 Earth twins (plus an additional $\sim$9 candidates)—consistent with the Stark et al. [122] baseline yields of 4–16 Earth twins for a multi-visit search (roughly equivalent to our targeted scenario), depending on astrophysical and systematic noise levels. Our Earth twin definition matters here to the extent that whereas Stark et al. [122] fixed $R = 1\ R_{\oplus}$, about half of our underlying Earth twins are smaller than this. Contrast ratio goes as R^2, so more of our simulated planets may be too faint to detect, compared to the earlier work.

3.5 Discussion

3.5.1 Model assumptions

We have made several simplifying assumptions throughout this numerical study. We now evaluate how damning these assumptions may be, and how they affect our results. Table 3–2 summarizes our sensitivity analysis.

Search volume. In a volume-limited survey, one must decide on a maximum survey distance, r_{max}. There is a trade-off between detection efficiency and Earth twin yield for a given value of r_{max} (figure 3–3). Whereas our baseline survey sets the search volume such that a star at $r = r_{\mathrm{max}}$ would have all of its Earth twins obscured by the IWA, we tested a simulation where the furthest star would be complete for Earth twins. We find that this assumption reduces the targeted false positive rate from 47% to 43%—not a very significant decrease—and this smaller volume may yield little-to-no Earth twins.

Stellar number density. We eschew rigour for analytical convenience in estimating the number of target stars in our search volume. The stellar number density parameterization from Bovy [15] is not designed for lower-mass stars (<1

	Blind				
	Stars visited	$N_\oplus$ total	$N_\oplus$ detected	$N_{\mathrm{un}\oplus,\mathrm{ETCZ}}$ detected	FPR (%)
Baseline	136	16.1	2.0	7.0	77
FGK stars	420	49.2	3.9	16.2	81
Log-normal R	136	12.2	1.5	4.5	75
Log-normal P	136	33.0	4.2	10.0	70
Nonzero e	136	16.2	2.1	7.1	77
Log-normal A*	136	16.3	2.3	7.4	76
$\lambda = 400$ nm	2126	246.1	30.4	108.2	78
$D = 4$ m	8	1.0	0.1	0.4	77
IWA $= 2\lambda/D$	235	28.1	3.6	12.1	77
OWA $= 2'$	136	16.2	2.1	7.4	78
$r_{\max} = a_{\oplus,\min}/\mathrm{IWA}$	18	2.1	0.9	2.9	76

	Targeted				
	Stars visited	$N_\oplus$ total	$N_\oplus$ detected	$N_{\mathrm{un}\oplus,\mathrm{ETCZ}}$ detected	FPR (%)
Baseline	136	16.2	5.3	4.7	47
FGK stars	434	49.5	10.9	13.9	56
Log-normal R	136	12.5	4.2	2.9	41
Log-normal P	136	32.9	11.0	9.4	46
Nonzero e	136	16.3	6.4	5.6	47
Log-normal A*	136	16.3	6.1	4.3	41
$\lambda = 400$ nm	2126	251.3	84.4	72.9	46
$D = 4$ m	8	1.0	0.3	0.3	46
IWA $= 2\lambda/D$	235	28.3	9.5	8.2	47
OWA $= 2'$	136	16.1	5.4	4.8	47
$r_{\max} = a_{\oplus,\min}/\mathrm{IWA}$	18	2.1	1.9	1.4	43

Table 3–2: Target list sizes, number of underlying Earth twins, yields of Earth twins and un-Earths in the Earth twin candidate zone, and false positive rates under model assumptions which are relaxed one at a time. The false positive rate is quite consistent across different assumptions, despite changes in yields and target list sizes. Note that for the bottom five rows, the survey visits a dramatically different number of stars. This is due to equation 3.12, where any stars with maximum Earth twin semi-major axis inside the IWA are discounted from the target list. Based on 10^5 simulated stars, where yields are scaled to a realistic number of targets (as listed in columns 2 and 7). At this level of Poisson noise, the reported yields and false positive rates are precise to about ± 0.2 and $\pm 2\%$, respectively.

$M_\odot$), and will overestimate number densities in that mass region.[7] Other sources of error would nevertheless dominate results.

Stellar spectral type. Our initial assumption was that all Earth twin host stars have mass $M_* = M_\odot$. However, F, G, and K stars may be optimistically classified as "Sun-like". The semi-major axis range within which a planet would receive Earth-like insolation is farther out for F stars and closer in for K stars; we therefore expect different Earth twin detectabilities, via changes in both planet/star contrast and obscuration. Here we evaluate how a realistic distribution of stellar masses would affect our results.

Our re-analysis is limited to stars at least as massive as the K5 spectral type. Habitable zone planets orbiting stars less massive than this—e.g., M-dwarfs—will not only have zero obliquity [59], but they will also be synchronously rotating [64]. Their climates are likely quite alien [117].

We let M_* have a power law distribution, $\mathrm{d}N/\mathrm{d}M_* \propto M_*^{-4.7}$ [15]. We choose a normalization such that the cumulative probability equals unity in the range $M_* = [0.67, 1.6]\ M_\odot$. Stellar luminosity is calculated by $L_*/L_\odot = (M_*/M_\odot)^4$. The values of $a_{\oplus,\mathrm{min}}$ and $a_{\oplus,\mathrm{max}}$ at star q are then scaled by the square root of $L_{*,q}$, which effectively ignores the planetary albedo dependence on wavelength [64].

[7] To get a more accurate number of G dwarfs, one should use an initial mass function below 1 $M_\odot$ and add the result to equation 3.13 above 1 $M_\odot$ (Bovy, pers. comm.). Because stellar number density is only important for absolute yield estimation, we skip this step.

Because $a_{\oplus,\max}$ sets the edge of the the search volume (equation 3.12), this means that the furthest K star probed for Earth twins is nearer than the furthest-probed F star. In other words, a star q is disqualified if $a_{\oplus,\max,q} > r_q \times$ IWA. We find that relaxing $M_* = M_\odot$ slightly increases the false positive rate, but this is probably not significant.

Planetary demographics. How appropriate is the assumption that radius and semi-major axis have log-uniform distributions? Estimating underlying distributions of exoplanets near 1 $R_\oplus$ and 1 AU is difficult because we have observed so few such planets. Extrapolation is required, such as in Petigura et al. [96], whose flat distribution we implement in this study.

More recent work [45, 61] extrapolates the distributions of radius and period using fewer assumptions than Petigura et al. [96]. For planets on >100-day orbits, large radii (10 $R_\oplus$) may occur less frequently than small radii (1 $R_\oplus$), but the discrepancy is smaller than it is for shorter periods. Within the errors, however, a flat distribution does not appear to be inconsistent with Foreman-Mackey et al. [45].

The radius distribution of short-period planets is bimodal [50, 137], but may be shaped by atmospheric loss via evaporation [81]. For planets in the habitable zone of G dwarfs in particular, the radius distribution is still poorly constrained. In any case, radius comes into the direct imaging signal as A^*R^2, where the apparent albedo A^* is unknown. Even a bimodal distribution would likely be smeared out by albedo variance.

Estimates of earth twin occurrence rate are directly tied to these period and radius distribution models. Petigura et al. [96] present an occurrence rate $\eta_\oplus = 5.7\%$, which we divide by their Earth bin volume to get a density, $\Gamma_\oplus = 0.12$. Foreman-Mackey et al. [45] update Petigura et al. [96] to find $\Gamma_\oplus = 0.02$, smaller by an order of magnitude, while Hsu et al. [61] find $\Gamma_\oplus = 1.6$, larger by an order of magnitude. We adopt the earlier value from Petigura et al. because it is based on log-uniform distributions in R and a, so we can apply a constant value of Γ to all planets in our simulation, and still not conflict with previous work. The true occurrence rate may lie somewhere between these two results.

If Γ is constant—that is, if planets occur at equal rates in every bin—then the detection efficiency and its variation over R and a are divorced from the actual value of $\Gamma_\oplus$, for a volume-limited search. We are free, then, to ignore whether $\Gamma_\oplus$ is closer to 0.02 or 0.12; its value is only needed to estimate yields.

However, if Γ is not constant and $\Gamma_\oplus$ is lower than its neighbouring bins [45], then our survey would yield more false positives. Or vice versa, if $\Gamma_\oplus$ is higher than its neighbours [61, 70].

We tested how non-uniform demographics change our results by implementing log-normal distributions for both R and P, with μ at the respective Earth value, and σ the width of one bin. The increased abundance of Earth twins means the false positive rate is lower by a handful of percentage points, excepting the targeted scenario for a log-normal P realization (since the a-a_{proj} degeneracy is trivial).

We also prescribe an overall upper limit of 4.5 $R_\oplus$ to the planets we generate (e.g., one e-folding above $R_{\oplus,\max}$). This may miss false positives with large radii and low albedo, or crescent phase. Hence, again, our results give a lower limit of the false positive rate.

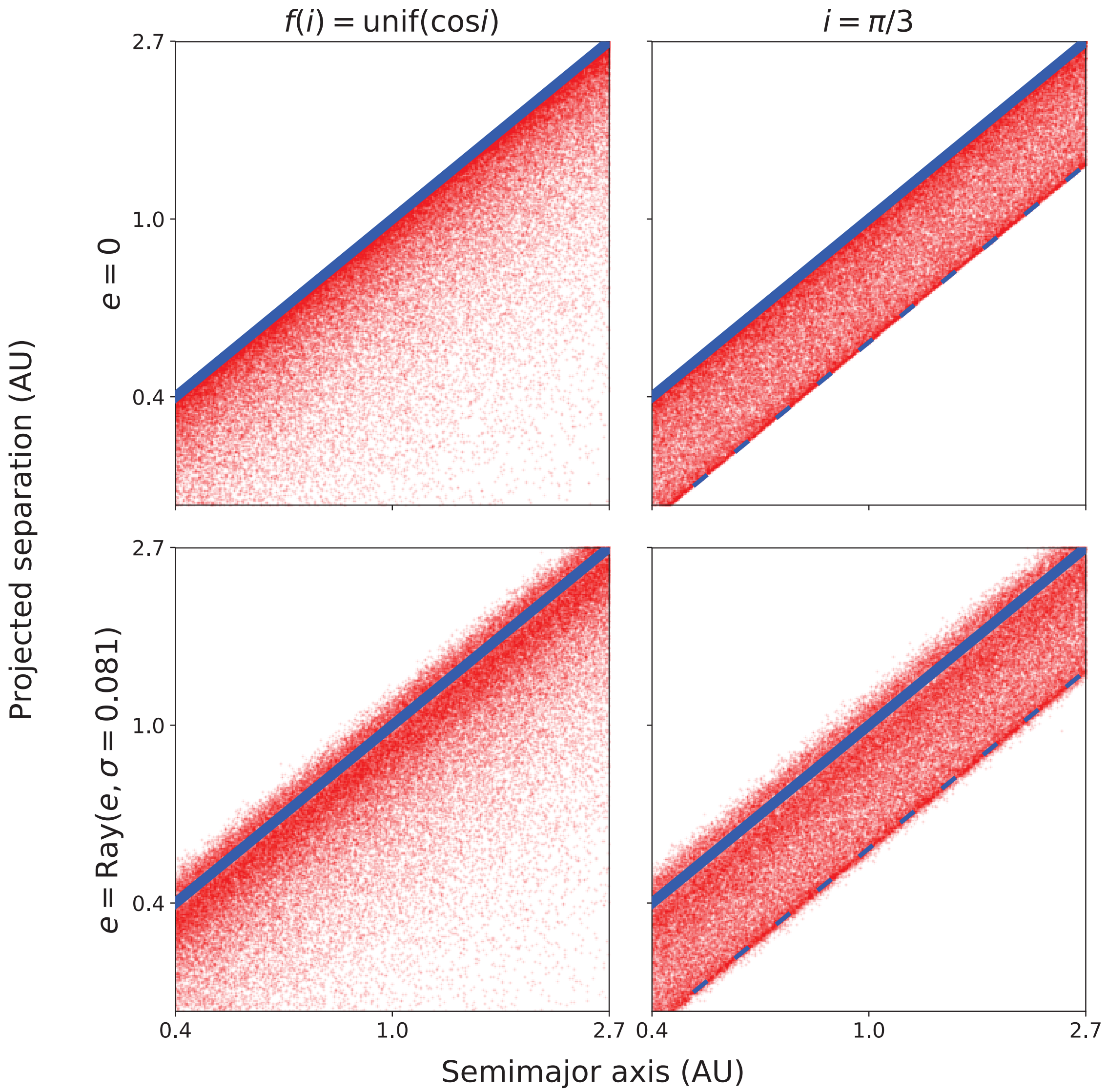

Figure 3–4: Density scatter plots showing the distribution of projected separation with semi-major axis for different assumptions about eccentricity and inclination distributions. The solid blue line indicates 1:1 correspondence, $a_{\rm proj} = a$. The dashed blue line shows $a_{\rm proj} = a\cos i$, which is the minimum $a_{\rm proj}$ for fixed inclination and circular orbits. The distribution of $a_{\rm proj}$ with a is bimodal for fixed inclination (right column) because the apparent orbital speed of the planet has minima at both $a_{\rm proj} = a$ and $a_{\rm proj} = a\cos i$, effectively piling-up planets at these four points on the orbit.

Orbital eccentricity. We have assumed circular orbits, but we know precious little about the eccentricity of sub-Neptunes in long-period orbits around Sun-like stars, let alone Earth twins.

To test how non-zero eccentricity affects our results, we ran a simulation where eccentricity is drawn from a Rayleigh distribution with dispersion $\sigma = 0.081$, as given by Shabram [114] for transiting planets. Although eccentricities are especially hard to measure for small planets, reports of eccentricity-period distributions consistently show peaks around $e \approx 0$, for both transiting and radial velocity planets [131].

We find that treating e as a random parameter results in a false positive rate of 77% for a blind survey and 47% for a targeted survey, indistinguishable from our fiducial, zero-eccentricity case. We posit that this is because inclination, not eccentricity, represents the first-order control on the distribution of projected separation with semi-major axis (figure 3–4). We therefore conclude that our analysis is robust to the assumption of circular orbits.

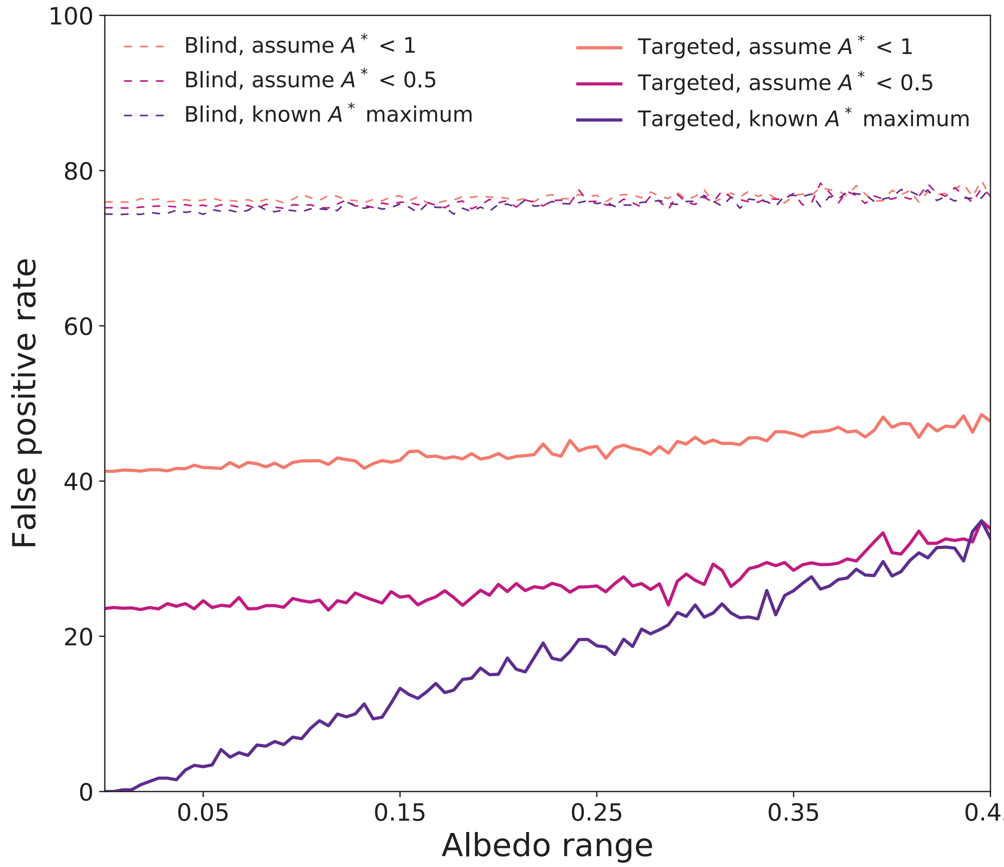

Figure 3–5: Effect of albedo distribution—and our knowledge thereof—on the false positive rate, or, the odds of an Earth twin candidate being an un-Earth. The x-axis is the range within which albedo is allowed to randomly vary *in the model*: the greatest range corresponds to $A^* \in [0.05, 0.5]$, and the smallest range to $A^* = 0.3$. Dashed lines represent searches for planets at random phase, while solid lines represent targeted searches. Colours show different assumed maximum albedos (e.g., the value of A^* in equation 3.15). Noise in this figure is due to model Poisson noise: because A^* is generated anew for each planet per albedo range increment, sometimes planets will be assigned new A^* values sufficiently low to diminish their planet/star contrasts below the instrument floor, which renders them undetectable. Targeted searches still have false positive rates of at least 1 in 2, unless all planets have the same albedo (albedo range of 0) and we know that universal albedo *a priori* (solid purple line).

Phase function and albedo. We have adopted the Lambertian phase curve throughout our analysis. Under this assumption, the light reflected by the planet's atmosphere is diffuse—it scatters in all directions. In reality, however, a planet's phase function will differ from the Lambertian model [20, 85]—for example, Titan is strongly forward-scattering and appears brighter at larger phase angles [51]. Our ignorance of exoplanet phase functions is largely encapsulated in the apparent albedo, which we allow to vary by an order of magnitude.

As we have stressed throughout this work, the albedo distribution of rocky planets is wholly unconstrained. Moreover, A^* may change as we observe different regions of the planet [30]. This variation is controlled by (i) the planet's rotation about its axis, (ii) the obliquity of that axis, and/or (iii) weather and seasons.

As for our assumptions about $A^*_{\rm min}$ and $A^*_{\rm max}$, hot Jupiters exhibit more than an order of magnitude range in albedo [60], despite being relatively simple planets: similar mass, size, composition, etc. There is therefore reason to believe that smaller, cooler planets, which are inherently more diverse, will exhibit a variety of different albedos.

In figure 3–5, we present the Earth twin false positive rate as a function of the underlying range of apparent albedo. The problem of unknown albedo is twofold: not only do we not know the albedos of individual planets, but we do not even know the albedo *distribution* of planets at 1 AU. Therefore, we are left with (i) our best guess for $A^*_{\rm max}$ (which affects the extent of the Earth twin candidate zone), as well as (ii) our luck in nature's range of A^* being on the small side.

The Earth twin false positive rate varies with both of these estimates. If every candidate planet had the same albedo and phase function *and* we knew the universal albedo and phase function *a priori*, then—and only then—would a targeted search return a 0% false positive rate, since the radius-albedo degeneracy would be broken. As the universe's underlying distribution widens, however, our knowledge of the albedo maximum gives us less and less of an advantage.

Table 3–2 shows that adopting an underlying normal distribution for A^* ($\mu = 0.3$, $\sigma = 0.1$) also reduces the false positive rate of a targeted search, in a similar way to shortening the range of A^*.

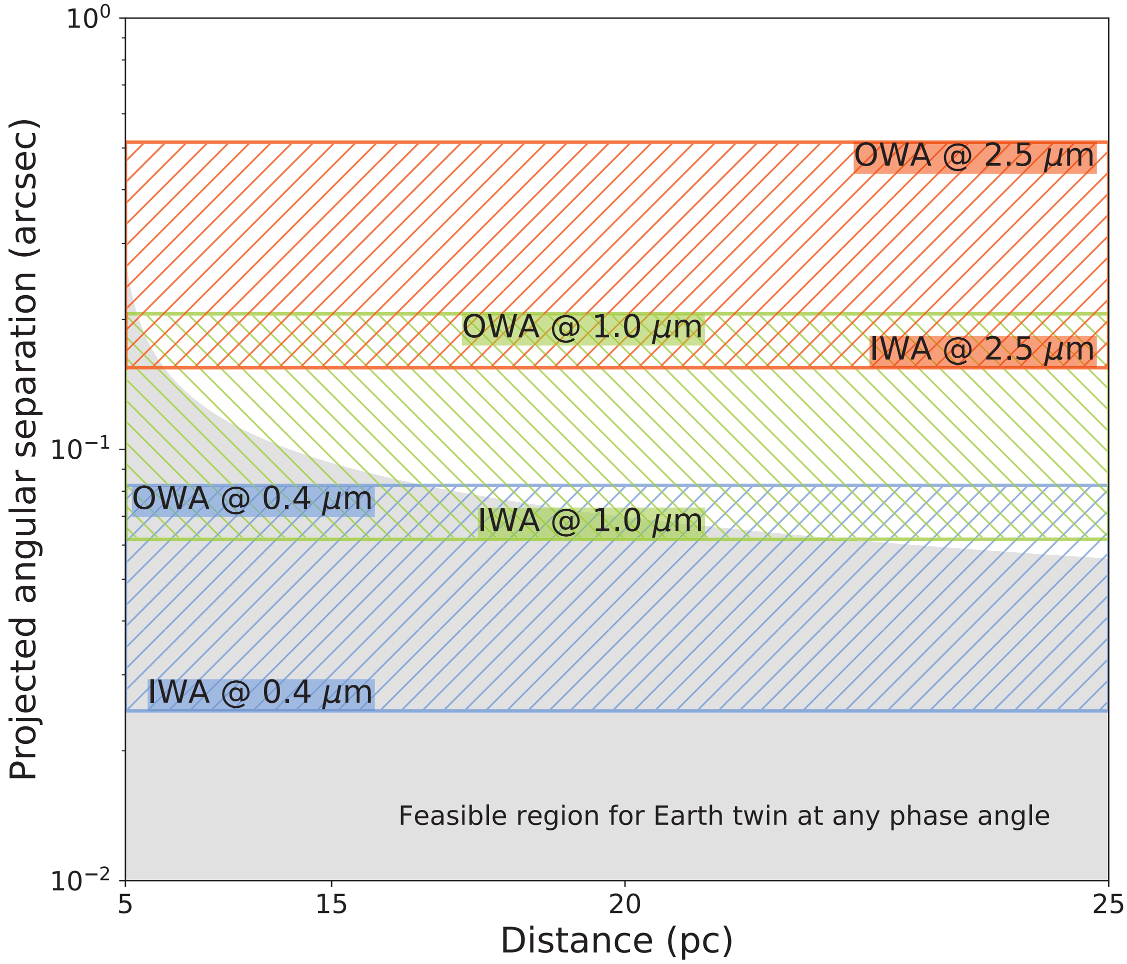

Figure 3–6: Inner and outer working angles at various wavelengths (horizontal lines), for a 10-m telescope with an IWA of $3\lambda/D$ and an OWA of $10\lambda/D$. Hatched regions represent where an exoplanet would be unobscured. The angular projected separation for an Earth twin, as a function of distance, is shown by the grey region. Targets are only visible at some wavelength if the grey swath intersects a wavelength's working angle box. The hatched regions have little-to-no overlap, meaning that no planets can be simultaneously imaged from 0.4 to 2.5 μm, and a full spectrum can only be stitched together for the very nearest and most inclined planets. Because the x-axis is scaled to constant volume per centimetre, this demonstrates that the vast majority of Earth twins have too tight a projected angular separation for longwave characterization.

Wavelength and working angles. We have mentioned, but not yet stressed, that inner and outer working angles depend directly on imaging wavelength. Shorter wavelengths will tighten the working angles, while longer wavelengths will push them to wider separations. The wavelength we choose to work with thus affects which planets are obscured and which are not. Our adoption of 1.0 μm dictates that planets are obscured more often than the 0.55-μm assumption of Stark et al. [122]. Indeed, Stark et al. [121, 123] require that planets are simultaneously detectable at 0.55 and 1.0 μm. Regardless, the false positive rate is roughly insensitive to both the wavelength and the working angles themselves (table 3–2).

If we want to spectroscopically characterize the atmospheres of planets we detect (i.e., do useful science), then we require observations at multiple bands. For full characterization, we would hope for a spectrum ranging from 400 nm in the shortwave (Rayleigh scattering), to 2.5 μm in the longwave (greenhouse gas absorption, e.g. methane).

Directly imaging a planet at multiple wavelengths is not trivial, however, due to chromatic working angles. We illustrate this in figure 3–6 by showing the projected angular separations at which an Earth twin might appear, overlain by the working angles at some different wavelengths.

If we want to *simultaneously* detect a planet at multiple wavelengths, then the regions bounded by the relevant IWAs and OWAs *and* the planet's angular separation must all overlap somewhere. As figure 3–6 shows, this is unfortunately not achievable for 400 nm and 2.5 μm, if OWA $= 10\lambda/D$ and IWA $= 3\lambda/D$.

Parallel coronagraphs, with different IWAs and OWAs, are a possibility for imaging more planets at such a range of wavelength bands.

Thus we may be forced to attempt stitching together observations taken at different phases, at least for planets on inclined orbits. This raises practical challenges, since $\phi(\alpha)$ varies with wavelength; phase variations are likely chromatic [22, 85]. Further—and this extends to all of Earth twin spectroscopy—we are chasing moving targets. The integration time required to characterize an Earth twin could be on the scale of months [107], and a planet on a 1-AU orbit will surely move during this time.[8] It may therefore be necessary to acquire orbital constraints before obtaining spectra.

Regardless, even with snapshots at several orbital phases, figure 3–6 illustrates that only the nearest ($r \lesssim 9$ pc) Earth twins are possibly observable both at 400 nm and 2.5 μm. Of the simulated Earth twins detectable at 400 nm, 23.9% are detectable at 1.0 μm at any phase, and only 0.6% at 2.5 μm.

One debatable solution is to use a starshade, rather than a coronagraph, to obtain spectra of Earth twin atmospheres. The IWA of a starshade depends on the starshade radius divided by the starshade-telescope distance, and its OWA is simply the field of view. This results in a greater unobscured range of separations. Starshades also have greater bandwidth, so obtaining a full spectrum requires

[8] A planet with a=1 AU at r=10 pc would move 5 pixels over a 30-day integration, assuming a Nyquist-sampled pixel scale and a 10-m telescope. The same planet at $r = 20$ pc would move 2.5 pixels.

fewer passes. However, because starshade slew time is long, fewer stars can be targeted, and starshades themselves pose different technical challenges.

Multiple observations

Our blind search model assumes one observation per star, while our targeted search assumes either precursor orbit constraints, or enough direct imaging visits per star to fully constrain planetary orbits. A realistic mission will fall between these endmembers—at a given point, we may have visited a star more than once, yet possibly not enough times to precisely know the semi-major axis of the hosted planet(s). This raises an interesting question: how does the false positive rate change with each additional visit to the same star? The answer requires knowing the most efficient timing of visits, an important area of future research. For now, we posit that our false positive rates reported for the blind and targeted scenarios represent upper and lower bounds, respectively.

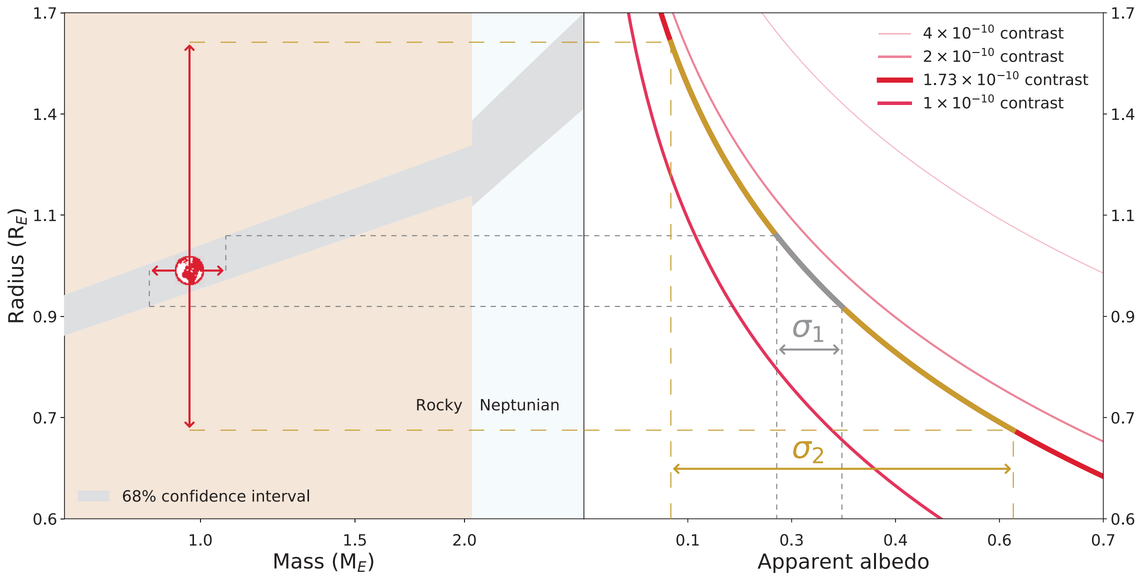

Figure 3–7: *Left:* Planetary mass-radius relation from Chen & Kipping [24]. Grey swath shows 68% confidence interval. Horizontal error bars are the hypothetical mass measurement error, here set at a very optimistic value of 10% (e.g., using 1 cm/s precision radial velocity [97]). Vertical error bars show a hypothetical radius constraint retrieved from a Rayleigh scattering spectrum [41]. The dashed lines show 1σ radius constraints, where grey lines correspond to the mass constraint and ochre lines correspond to the spectral retrieval constraint. *Right:* radius-albedo degeneracy at a constant planet/star contrast of 1.73×10^{-10} (bold line), which corresponds to an Earth twin at quadrature and 1 AU separation. Other lines show different planet/star contrasts for the same phase and separation. The error on radius, as estimated from mass or from spectral retrieval, directly propagates to an error on albedo. We might then estimate albedo to within roughly ± 0.05 (σ_1) or ± 0.25 (σ_2), respectively, for planets with Earthlike albedo and radius.

3.5.2 Breaking the radius-albedo degeneracy

We consider two possible routes to constraining planetary albedo (figure 3–7). One route is to choose targets whose masses are known from radial velocity or astrometry surveys [97, 116, 10, 42, 130]. We can use a mass-radius relation [24, e.g.,] to estimate the planet's radius from its mass. This is a risky endeavour, as current mass-radius relations are necessarily for short-period planets and therefore may not be representative of Earth twins. A corollary benefit of targeting known-mass planets is that their orbits would have been constrained along with mass. This would inform us of which stars to target and when to look.

The second route takes advantage of Rayleigh scattering. Feng et al. [41] showed that modeled Rayleigh scattering spectra are independent of surface albedo, and could therefore constrain radius. In theory, if we measure the Rayleigh scattering spectrum of a planet at known phase, then we can estimate its radius.

This retrieval is more complicated for an atmosphere with clouds. However, the longer atmospheric path-lengths at crescent phase mean that surface and cloud scattering are less important at these phase angles. Thus, reflected light at crescent phase is—in principle—closer to pure Rayleigh scattering, and hence might constrain radius, even for cloudy atmospheres.

Figure 3–7 shows that a 10% constraint on mass would propagate to approximately a $\pm 0.1\ R_\oplus$ constraint on radius and a ± 0.05 constraint on albedo, for Earthlike planets at 1 AU, and that a 50% radius constraint from a Rayleigh scattering spectrum would propagate to an ± 0.25 constraint on albedo. A precise value of σ_{A*} is not reported because this error would be dominated by systematic errors; e.g., using a mass-radius relationship for short period planets.

3.6 Conclusions

We have performed Monte Carlo simulations of reflected light direct imaging surveys adopting a simple telescope model. Our main finding is: if we image stars at random, $\sim$77% of the detected planets that appear Earthlike in separation and planet/star contrast will in fact not be Earth twins. Meanwhile, $\sim$88% of Earth twins go undetected within our search volume of 22.6 pc, although this depends on model assumptions; namely, the maximum survey distance in our volume-limited survey.

We can double the chances that detected Earth candidates are true Earth twins—and triple the chances of seeing Earth twin planets, on average—by only targeting known planets. Yet even then we cannot do better than a $\gtrsim$50% false positive rate, as our capacity to know whether a planet is an Earth twin is set by our knowledge of the albedo distribution of rocky planets at large semi-major axes. These two estimates of the false positive rate represent endmember search scenarios, in which we either know nothing or everything about the orbits of the imaged planets. The false positive rate of a realistic direct imaging mission would fall in between these values.

Our results are robust to working angle geometry (including imaging wavelength), to the assumption of non-circular orbits, to the inclusion of F and K stars, and to the underlying radius, period, and albedo distributions of planets.

Breaking the radius-albedo degeneracy should be a focus of research before choosing Earth twin candidates for costly spectroscopic characterization. We may be able to constrain a planet's radius from its mass, motivating cooperation between direct imaging and radial velocity and astrometry.

3.7 Acknowledgements

This work is supported by the McGill Space Institute and the Technologies for Exo-Planetary Science training program. We show our gratitude to the LUVOIR STDT for their useful conversation, to the Exoclipse meeting attendees and organizers for the feedback received on a preliminary presentation of this work, to M. Marley and T. Robinson for enlightening discussion on the radius-albedo degeneracy, and to an anonymous referee, whose comments greatly improved the scientific quality of this manuscript. Lastly, NBC acknowledges the support of the Canadian Space Agency towards attending LUVOIR meetings.

Randomly-generated planetary parameters						
Symbol	Min	Max	Units	Description	Probability distribution	Eqn.
R	0.6	4.5	$R_\oplus$	Planetary radius	Uniform in $\ln(R)$	3.5
a	0.37	2.72	AU	semi-major axis	Uniform in $\ln(a)$	3.6
ξ	0	2π	rad	Orbital phase	Uniform	3.7
i	0	$\pi/2$	rad	Orbital inclination	Uniform in $\cos(i)$	3.8
A*	0.05	0.5	-	Planetary apparent albedo	Uniform	3.10
r	0	22.6	pc	Distance between star system and observer	Uniform in r^2	3.11

Derived planetary parameters			
Symbol	Units	Description	Eqn.
ε	-	Planet/star contrast ratio	3.1
$\phi_L(\alpha)$	-	Lambertian phase function	3.2
α	rad	Phase angle between planet and observer	3.3
a_{proj}	AU	Projected separation	3.4
ε'	-	Phase-normalized planet/star contrast ratio	3.15

Free model parameters			
Symbol	Value	Units	Description
$\varepsilon_{\min}$	1.0×10^{-10}	-	Coronagraph raw planet/star contrast ratio
$R_{\oplus,\min}$	0.6	$R_\oplus$	Minimum radius for Earth twin classification
$R_{\oplus,\max}$	1.6	$R_\oplus$	Maximum radius for Earth twin classification
$a_{\oplus,\min}$	0.72	AU	Minimum semi-major axis for Earth twin classification
$a_{\oplus,\max}$	1.40	AU	Maximum semi-major axis for Earth twin classification
$\Gamma_\oplus$	0.119	nat^{-2}	Earth twin occurrence rate density
M_*	1	$M_\odot$	Mass of host star
D	10	m	Telescope primary aperture diameter
λ	1.0	μm	Imaging wavelength
N_{in}	3	-	Number of λ/D at coronagraph inner working angle
N_{out}	10	-	Number of λ/D at coronagraph outer working angle

Table 3–3: Definitions of symbols used in this text. Listed values correspond to the fiducial case; many of these parameters are varied in our sensitivity analysis.

Chapter 4
Additional discussion

This chapter embarks on an exploratory assortment of research questions not yet published.

4.1 Other ways to discriminate Earth twins

A next step in my research program is to incorporate parameters other than single-band brightness contrast into the false positive model. This section preempts an incubating collaboration between myself and the group headed by Prof. Victoria Meadows at the NASA Astrobiology Institute/University of Washington, which I will be visiting this spring.

Guimond & Cowan [57, see chapter 3] distinguish true positives from false ones based on: (i) the maximum planet-star contrast that an Earth twin could have, from which radius is derived, and (ii) the allowable projected separation, from which semi-major axis is derived. Yet Krissansen-Totton et al. [73] have shown that colours—that is, this brightness contrast as ratios of two wavelength bands—are viable parameters for this type of planetary classification. They calculate the two optimal colours that best separate Earth twins from other planets in colour-colour space. Colour tells us about surface features and/or the large-scale shape of atmospheric absorption.

Thus we might extend the model of Guimond & Cowan [57] to include observations of hypothetical exoplanets at these optimal colours, asking the question: given a projected separation and a location in colour-colour space, what is the probability that a detected planet is an Earth twin?

However, there are several flaws in colour analysis, namely that colours of planets vary with phase angle [85]. Further, a look to Archaean Earth attests that terrestrial planets come with myriad surface qualities. We do not have a good enough theoretical understanding to predict Earth twin colours [86]. Even if we do separate dots into groups in colour-colour space [73], our lack of planetary controls will impede us in classifying these dots. In the least, however, colours could set apart Earth twins from sub-Neptunes and from astrophysical false positives. Photometry could also be expanded to low-resolution spectra, likely more discriminating than colours, but with higher observation cost.

A parallel approach, perhaps, is to focus on phase curves of these planets. The work thus far uses only a Lambertian phase function, but this should be a weak assumption for terrestrial planets. HAYSTACKS is a model of spatial and spectral information for the solar system, designed to simulate direct imaging observations of exoplanets [104]. By using output phase curves from this model, instead of the Lambertian, one could produce more realistic brightness contrasts for rocky planets; hypothetically, such considerations could improve the false positive rate. Robinson [105] showed that planets with oceans appear brighter at crescent phase due to glint, as a notable illustration. Yet the setback, again, lies in our poor constraints on the variability of phase curves for terrestrial planets.

4.2 Orbital constraints from multi-epoch imaging

Here I wax mathematic on the unheeded problem of constraining these directly-imaged Earth twins' orbits.

In current-era direct imaging, most planets we find are at wide separations with >1000-day periods. On a pixel scale, the target hardly moves in a mission lifetime[1] —constraining the orbit such that we can find it again has not been an issue, so the art of orbit-constraining is somewhat auxiliary to detection tactics. The same planets on Earthlike orbits, however, would be sure to move a couple pixels per month. So in these cases we have an unprecedented problem.

The work in chapter 3 does not take discrete revisits into account; it assumes either one or infinite visits as the endmember cases. A real mission will have an average number of visits per star that is greater than one, less than infinity.

Orbit-constraining could come from multi-epoch direct imaging in this way, or it could come from other surveys by different detection methods. WFIRST will target known radial velocity planets, for example—given radial velocity measurements (which constrains neither inclination nor longitude of the ascending node), what is the optimal scheme to most efficiently nail the planet's orbital parameters? This is an unsolved problem.

[1] Assuming typical direct imaging target properties, $a = 10$ AU, $r = 30$ pc, and a Nyquist-sampled pixel scale

4.2.1 Marginal improvement per epoch

The relevant question is: how does the posterior on orbital parameters change with more than one direct imaging observation? Given a planet with measured $a_{\rm proj}$ and ε from one image, one can construct a posterior distribution on a, i, ξ. Appendix A describes the analytic probability distribution of ε. One can treat two images as two independent measurements to get two posteriors, etc. These posteriors would then be multiplied together, and quantitatively compared to the original single-image result. Including photometric colours as a measured parameter could enact a similar approach. That is, given colours and $a_{\rm proj}$, what are the posterior distributions on orbital parameters, and how do they change with each image?

Yet this has not presumed the planet is on a Keplerian orbit. In theory, such laws would serve as additional constraints, so the orbit could be fully described faster. Alternatively, one could also incorporate posteriors gleaned from phase curve models into these statistics. It is an open question whether any of this is actually useful, however.

4.2.2 The trade-off

One less star is visited for each star *re*visited, for a given mission length. Thus, it is not obvious that a star should always be revisited as many times as possible. Here we show a first attempt to quantify this trade-off in terms of Earth twin yields.

The average exposure time per star, $\langle\tau\rangle$, increases with search volume:

$$\langle\tau\rangle = \frac{3}{5}\tau_0 \left(\frac{r_{\mathrm{max}}}{r_0^2}\right)^2, \tag{4.1}$$

where r_{max} is the maximum distance from Earth, and r_0, τ_0 are boundary conditions. We can substitute r_{max} for a total number of stars surveyed, N_*, given a stellar number density η_*,

$$\langle\tau\rangle = \frac{3}{5}\frac{\tau_0}{r_0^2}\left(\frac{3N_*}{4\pi\eta_*}\right)^{\frac{2}{3}}. \tag{4.2}$$

The total mission exposure time, τ_{tot}, can then be parameterized as

$$\tau_{\mathrm{tot}} = \langle\tau\rangle N_*, \tag{4.3}$$

which can be rearranged in terms of N_* and log-transformed (for convenience),

$$\log N_*(\tau_{\mathrm{tot}}) = \frac{3}{5}\log(\tau_{\mathrm{tot}}) - \frac{3}{2}\log\left[\frac{3\tau_0}{5r_0^2}\left(\frac{3}{4\pi\eta_*}\right)^{\frac{2}{3}}\right]. \tag{4.4}$$

If a dot (planet) is detected on blind luck within the Earth twin candidate zone, our options are to (I) continue to visit this star k times until the orbital parameters of that planet are constrained, or (II) move on and hope to find more dots around other, increasingly distant stars. Both cases assume no precursor observations, so orbital information is only obtained via subsequent direct imaging visits.

The Earth twin yield is proportional to the number of stars visited, N_*, times the Earth twin occurrence rate, $\eta_\oplus$, times the fraction of underlying candidates that are detected, f_{det}, times the true positive rate (the fraction of detected candidates that are Earth twins). Detection efficiency depends on r_{max} and therefore N_*,

$$\log f_{\rm det} = \log(a) + b\log(N_*), \tag{4.5}$$

where we find $a = 1.008$ and $b = -0.844$ for blind searches, using `numpy polyfit`. Meanwhile, true positive rate is independent of $r_{\rm max}$ for large search volumes ($r_{\rm max} > 8$ pc).

In case (I), the benefit of constraining the orbit lies only in increasing the true positive rate; that is, greater likelihood that the dot you detected is an Earth twin:

$$\log Y_{\oplus,I}(N_*) \propto \log N_* + \log \eta_\oplus + \log f_{\rm det,blind}(N_*) + \log {\rm TPR}_{\rm targeted}. \tag{4.6}$$

We use the detection efficiency for blind searches here because we assume that the star only continues to be targeted if the dot is seen on the first visit, which is blind by definition.

Otherwise, in case (II), we can target k extra stars for every dot constrained in case (I), although our true positive rate is smaller:

$$\log Y_{\oplus,II}(N_*) \propto \log[N_*+kY_{\oplus,I}(N_*)]+\log \eta_\oplus+\log f_{\rm det,blind}[N_*+kY_{\oplus,I}(N_*)]+\log {\rm TPR}_{\rm blind}. \tag{4.7}$$

In this equation, N_* represents the number of stars targeted in case (I).

Comparing $\log Y_{\oplus,II}(\tau_{\rm tot})$ and $\log Y_{\oplus,I}(\tau_{\rm tot})$, for $k = 10$ and assuming 30-second exposures for targets at 10 pc, we get that $Y_{\oplus,II} > Y_{\oplus,I}$ for all values of $\tau_{\rm tot}$. This simplistic approach implies that direct imaging may be wasted if depended upon to constrain a planet's orbit. The optimal strategy is probably to target *a priori* known planets with direct imaging, based on a precursor astrometry or radial velocity mission.

Not considered in this analysis is the fact that case (I) will also return more false positives, which will entail greater time spent during the characterization stage.

4.3 Mapping rocky worlds with LUVOIR

This section is adapted from a science case first-authored by Claire Guimond, submitted to the LUVOIR Interim Report.

The very large aperture of LUVOIR will enable reflected light surface mapping and spin determination for terrestrial planets [94, 92, 28, 66, 67, 48]. Previous mapping papers have adopted the optimistic 1% photometric uncertainty (S/N of 100) for 1-hr integrations. For a 15-m telescope, this will only be possible for a super-Earth at <1 pc. However, Cowan et al. [28] claimed they could do essentially the same science with 3% photometry in 1-hr integrations (24 data per rotation, each of S/N=33).

As figure 4–1 shows, for an Earth twin at 10 pc, we can only expect an S/N of $\sim$10 with one rotation, but for more slowly rotating planets and/or larger radii, this value can double or triple. Further, decreasing the time resolution (i.e., longitudinal sample rate) by a factor of 16 increases the per-integration S/N by a factor of 4—this would set the number of pixels in the final map. Stacking multiple epochs of observations can be problematic, as clouds strongly influence reflected light fluxes, and these atmospheric features are prone to change between epochs [92]. Thus only with a 15-m class space telescope such as LUVOIR can we start to map super-Earth exoplanets. For the smallest targets, only spin orientation and low-resolution longitudinal maps will be retrievable.

At first, perhaps only one or two super-Earths will be mappable—but the impact on knowledge should be massive. Specifically, for example, Kawahara & Fujii [67] show that the spatial distribution of vegetation on our planet can be retrieved in simulated exoplanet observations by looking across the *red-edge*, or, the ratio of a certain two wavelength bands which is used widely in remote sensing of Earth by satellites. The red-edge arises out of the fact that chlorophyll in terrestrial plants absorbs strongly in green wavelengths, but is almost transparent at wavelengths just longer than this, so the ratio of reflectance between these bands carries information about vegetation occurrence. The red-edge (actually, extraterrestrial analogs comprising different wavelength bands) has previously been proposed [112] as a workable biosignature, but the ability to resolve this signal spatially would minimize confusion from other surface types on the planet. Hence, at best, we could be observing direct evidence of chlorophyll analogs on exoplanets. At worst, we will obtain controls for astrobiological false positives.

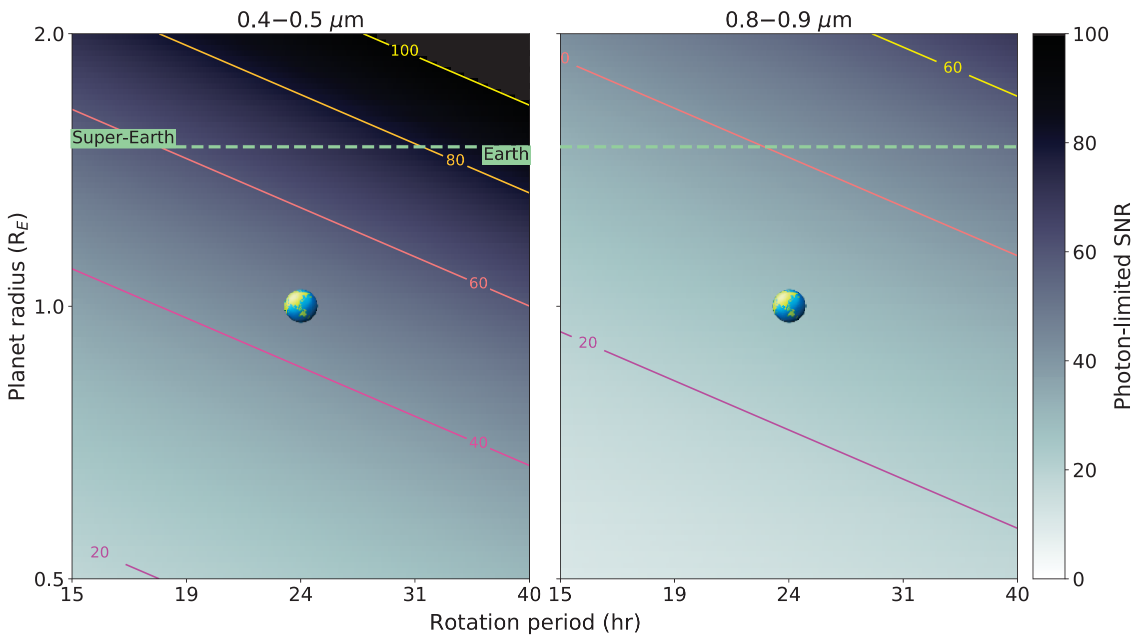

Figure 4–1: Signal-to-noise ratio at the poisson limit for two bandpasses as a function of rotation period and planet radius, for a planet at 10 pc with a semi-major axis of 1 AU and geometric albedo of 0.3, and a nominal telescope diameter of 15 m and coronagraph throughput of 15%.

Chapter 5
Summary and general conclusions

The work's conclusion-at-large is that if we directly image a dot that looks Earth-like, it is likely unEarth-like, in the end. This was shown in a Monte Carlo analysis, where synthetic planet parameters were drawn from distributions, their detectabilities were evaluated, and the yields of Earths and unEarths were compared.

This analysis runs parallel to the literature on exoplanetary habitability. While a planet's capacity to support life is ill-defined and model-dependent—for the forseeable future—we instead focus on the low-hanging observable fruit, brightness contrast and separation. Sooner or later, understanding habitability will need the characterization of rocky planet atmospheres.

Roads for future work include the investigation of photometric colours and phase curves, the optimization of direct imaging revisits, and the laying of theoretical groundwork for exo-cartography. Particularly low-hanging fruits are posteriors on other parameters: they could maybe abate the false positive rate, or else we rule them out and linger on.

APPENDIX A — Analytic methodology redux

If planetary demographics are simple analytic functions, then in theory we might be able to describe the false positive rate purely by analysis. This requires writing probability density functions of the two observables, ε and a_{proj}. Then, under the simplified assumption that these parameters are random independent variables for a given planet,[1] we could formulate a likelihood: given an observed ε and a_{proj}, what is the most likely R and a, and thus, how likely is the planet to be an Earth twin? This section demonstrates the beginning of such a pursuit.

The planet/star contrast ratio ε depends on geometric albedo A_g, phase function $\phi(\alpha)$, planet radius R_p, and semi-major axis a,

$$\varepsilon = A_g \phi(\alpha) \left(\frac{R_p}{a} \right)^2 . \tag{5.1}$$

If the planet is imaged at quadrature, $\phi(\alpha) = 1/\pi$ for a Lambertian phase function. Then for constant A_g, the value of ε depends on two variables, R_p and a. We are interested in the probability density function (p.d.f.) of ε, $\Pr(\widetilde{\varepsilon} \in (\varepsilon, \varepsilon + \mathrm{d}\varepsilon)) = f_{\widetilde{\varepsilon}}(\varepsilon)\mathrm{d}\varepsilon$. Hereafter, we use $\widetilde{\varepsilon}$ to denote a random outcome of contrast ratio, and ε the continuous real variable. We know the p.d.f. of $\ln R_p$ and $\ln a$. We can derive $f_{\widetilde{\varepsilon}}(\varepsilon)$ by first performing two single-variable transforms to convert $f_{\widetilde{\ln R_p}}(\ln R_p)$ and

[1] This is certainly a lie.

$f_{\widetilde{\ln a}}(\ln a)$ to $f_{\widetilde{R_p}}(R_p)$ and $f_{\widetilde{a}}(a)$, and then performing one two-variable transform to convert $f_{\widetilde{R_p}}(R_p)$ and $f_{\widetilde{a}}(a)$ into $f_{\widetilde{\varepsilon}}(\varepsilon)$. The single-variable transform method proceed as follows. Suppose an independent random variable has p.d.f. $f_{\widetilde{x}}(x)$ with support A. The function $y(x)$ is a 1-1 transformation of A onto B. This has the inverse $x(y)$. We will state without proof that the p.d.f. of y is

$$f_{\widetilde{y}}(y) = |x'(y)| f_{\widetilde{x}}[x(y)], \quad y \in B. \tag{5.2}$$

Starting with the simplest case, we derive the p.d.f. of R_p, knowing that $f_{\widetilde{\ln R_p}}(\ln R_p)$ is uniform,

$$f_{\widetilde{\ln R_p}} = \frac{1}{\ln\left(R_{\max}/R_{\min}\right)}, \quad \ln R_p \in [\ln R_{\min}, \ln R_{\max}]. \tag{5.3}$$

where $R_{\min}, R_{\max}$ are the upper and lower boundaries of the parameter space in which we are searching for planets. Let $x = \ln R_p$ and apply the transform $y = e^x$. This is a monotonic function with inverse $x = \ln y$. Thus we have $x'(y) = 1/y$ and, because the original p.d.f. is equal to a constant, $f_{\widetilde{x}}[x(y)] = 1/\ln\left(R_{\max}/R_{\min}\right)$. The p.d.f. of $R_p = y$ follows from (5.2),

$$\begin{aligned} f_{\widetilde{y}}(y) &= \frac{1}{y} \times \frac{1}{\ln\left(R_{\max}/R_{\min}\right)}, \quad y \in [y(x_{\min}), y(x_{\max})] \\ f_{\widetilde{R_p}}(R_p) &= \frac{1}{R_p} \times \frac{1}{\ln\left(R_{\max}/R_{\min}\right)}, \quad R_p \in [R_{\min}, R_{\max}]. \end{aligned} \tag{5.4}$$

The final step is to normalize the new p.d.f., by which the area under the cumulative probability must be unity:

$$\begin{aligned} C \times \int_{R_{\min}}^{R_{\max}} \frac{1}{\ln\left(R_{\max}/R_{\min}\right)} \frac{1}{R_p} \, \mathrm{d}R_p &= 1 \\ C \times \frac{1}{\ln\left(R_{\max}/R_{\min}\right)} \left[\ln\left(\frac{R_{\max}}{R_{\min}}\right)\right] &= 1 \\ C &= 1 \end{aligned} \tag{5.5}$$

Next, we derive the p.d.f. of a. Again, our original function comes from the fact that a is uniform in its logarithm:

$$f_{\widetilde{\ln a}} = \frac{1}{\ln\left(a_{\max}/a_{\min}\right)}, \quad \ln a \in [\ln a_{\min}, \ln a_{\max}]. \tag{5.6}$$

Repeating the process as above, let $x = \ln a$ and apply the transform $y = e^x$, with inverse $x = \ln y$. The form of the transformed p.d.f. is exactly the same, with normalization constant $C = 1$.

$$\begin{aligned} f_{\widetilde{y}}(y) &= \frac{1}{y} \times \frac{1}{\ln\left(a_{\max}/a_{\min}\right)}, \quad y \in [y(x_{\min}), y(x_{\max})] \\ f_{\widetilde{a}}(a) &= \frac{1}{a} \times \frac{1}{\ln\left(a_{\max}/a_{\min}\right)}, \quad a \in [a_{\min}, a_{\max}]. \end{aligned} \tag{5.7}$$

Now that we know $f_{\widetilde{R_p}}(R_p)$ and $f_{\widetilde{a}}(a)$, we can find $f_{\widetilde{\varepsilon}}(\varepsilon)$, where $\varepsilon = \varepsilon(R_p, a)$. The two variable transformation method is analogous to the single-variable case. Suppose two independent random variables have joint p.d.f. $f_{\widetilde{x_1,x_2}}(x_1, x_2)$ with support A. For completeness, we require two new variables onto which we transform A; $y_1(x_1, x_2)$ and $y_2(x_1, x_2)$. There exists an inverse transformation, $x_1(y_1, y_2)$ and $x_2(y_1, y_2)$. Now let the determinant J—analogous to $x'(y)$ and given by

$$J = \begin{vmatrix} \frac{\partial x_1}{\partial y_1} & \frac{\partial x_1}{\partial y_2} \\ \frac{\partial x_2}{\partial y_1} & \frac{\partial x_2}{\partial y_2} \end{vmatrix} \tag{5.8}$$

—be the Jacobian of the inverse transformation, assuming the partial derivatives are continuous over the support. The joint p.d.f. of y_1, y_2 is

$$f_{\widetilde{y_1,y_2}}(y_1, y_2) = |J| f_{\widetilde{x_1,x_2}}[x_1(y_1, y_2)], x_2(y_1, y_2)], \quad y_1, y_2 \in B. \tag{5.9}$$

In our case, however, we are only interested in the p.d.f. of one of these variables, rather than a joint p.d.f. Thus we integrate out y_2 to find the marginal p.d.f. of y_1,

$$f_{\widetilde{y_1}}(y_1) = C \times \int_{y_{2,\min}}^{y_1} f_{\widetilde{y_1,y_2}}(y_1, y_2)\, \mathrm{d}y_2. \tag{5.10}$$

where the normalization constant C is likewise found by setting the integral of this p.d.f. (the cumulative distribution) to unity. Now we demonstrate the transformation of $f_{\widetilde{R_p,a}}(R_p, a)$ into $f_{\widetilde{\varepsilon}}(\varepsilon)$. First we write the joint p.d.f. to be transformed—if $\widetilde{x_1}$ and $\widetilde{x_2}$ are independent, their joint probability density $f_{\widetilde{x_1},\widetilde{x_2}}(x_1, x_2)$ is equal to $f_{\widetilde{x_1}}(x_1) f_{\widetilde{x_2}}(x_2)$. Although this may not be true for R_p and a, we will make this assumption for simplicity. So

$$f_{\widetilde{R_p,a}}(R_p, a) = \left(\frac{1}{R_p} \frac{1}{\ln\left(R_{\max}/R_{\min}\right)}\right) \left(\frac{1}{a} \frac{1}{\ln\left(a_{\max}/a_{\min}\right)}\right), \quad R_p \in [R_{\min}, R_{\max}], a \in [a_{\min}, a_{\max}]. \tag{5.11}$$

Let

$$\begin{aligned} y_1 &= A_g \phi \left(\frac{R_p}{a}\right)^2, \quad y_1 \in [y_1(R_{\min}, a_{\min}), y_1(R_{\max}, a_{\max})] \\ y_2 &= a, \quad y_2 \in [y_2(R_{\min}, a_{\min}), y_2(R_{\max}, a_{\max})] \end{aligned} \tag{5.12}$$

where y_2 is chosen such that solving for its inverse is trivial. Find the inverses:

$$\begin{aligned} R_p(y_1, y_2) &= \sqrt{\frac{y_1}{A_g \phi} y_2} \\ a(y_1, y_2) &= y_2. \end{aligned} \tag{5.13}$$

Calculate the determinant:

$$\begin{aligned} J &= \begin{vmatrix} \frac{\partial R_p}{\partial y_1} & \frac{\partial R_p}{\partial y_2} \\ \frac{\partial a}{\partial y_1} & \frac{\partial a}{\partial y_2} \end{vmatrix} \\ &= \begin{vmatrix} \frac{\partial R_p}{\partial y_1} & \frac{\partial R_p}{\partial y_2} \\ 0 & 1 \end{vmatrix} \\ &= \frac{\partial R_p}{\partial y_1} \\ &= \frac{y_2}{2 \left(A_g \phi\right)^{\frac{1}{2}}} y_1^{-\frac{1}{2}} \end{aligned} \tag{5.14}$$

We substitute (5.13) into (5.11), and substitute this result and (5.14) into (5.9) to find the joint p.d.f.:

$$\begin{aligned} f_{\widetilde{y_1, y_2}}(y_1, y_2) &= \left(\left| \frac{y_2}{2 \left(A_g \phi\right)^{\frac{1}{2}}} y_1^{-\frac{1}{2}} \right| \right) \left(\frac{1}{\sqrt{y_1 / \left(A_g \phi\right) y_2}} \frac{1}{\ln\left(R_{\max}/R_{\min}\right)} \right) \left(\frac{1}{y_2} \frac{1}{\ln\left(a_{\max}/a_{\min}\right)} \right) \\ &= \frac{1}{2 \ln\left(R_{\max}/R_{\min}\right) \ln\left(a_{\max}/a_{\min}\right) y_1 y_2}, \quad y_1 \in [y_1(R_{\min}, a_{\min}), y_1(R_{\max}, a_{\max})], \\ &\qquad\qquad y_2 \in [y_2(R_{\min}, a_{\min}), y_2(R_{\max}, a_{\max})], \end{aligned} \tag{5.15}$$

in which the absolute value can be simplified because, with our chosen variables, y_1 (equivalent to ε) and y_2 (equivalent to a) are always positive. The final step is to integrate out y_2 from the joint p.d.f,

$$\begin{aligned} f_{\widetilde{y_1}}(y_1) &= \frac{1}{2\ln\left(R_{\max}/R_{\min}\right)\ln\left(a_{\max}/a_{\min}\right)y_1}\int_{\varepsilon_{\min}}^{y_1}\frac{1}{y_2}\mathrm{d}y_2 \\ &= \frac{\ln\left(y_1/\varepsilon_{\min}\right)}{2y_1}, \quad y_1 \in \left[y_1(R_{\min}, a_{\min}), y_1(R_{\max}, a_{\max})\right]. \end{aligned} \tag{5.16}$$

Thus the contrast ratio p.d.f. has the form

$$f_{\widetilde{\varepsilon}}(\varepsilon) = C \times \frac{\ln\left(\varepsilon/\varepsilon_{\min}\right)}{2\varepsilon}, \quad \varepsilon \in \left[\varepsilon(R_{\min}, a_{\min}), \varepsilon(R_{\max}, a_{\max})\right] \tag{5.17}$$

To normalize this p.d.f., we set the total cumulative probability equal to 1:

$$\begin{aligned} C\int_{\varepsilon_{\min}}^{\varepsilon_{\max}}\frac{\ln\left(\varepsilon/\varepsilon_{\min}\right)}{2\varepsilon}\mathrm{d}\varepsilon &= 1 \\ \frac{C}{2}\left[\frac{1}{2}\left(\ln\frac{\varepsilon_{\max}}{\varepsilon_{\min}}\right)^2 - \left(\ln\frac{\varepsilon_{\min}}{\varepsilon_{\min}}\right)^2\right] &= 1 \\ C &= \frac{4}{\left(\ln\frac{\varepsilon_{\max}}{\varepsilon_{\min}}\right)^2}. \end{aligned} \tag{5.18}$$

The same approach can apply to a probability distribution of a_{proj}.

References

[1] E. Agol. Rounding up the wanderers: optimizing coronagraphic searches for extrasolar planets. *Monthly Notices of the Royal Astronomical Society*, 374:1271–1289, February 2007.

[2] E. Agol and D. C. Fabrycky. *Transit-Timing and Duration Variations for the Discovery and Characterization of Exoplanets*, page 7. 2017.

[3] G. Arney, N. Batalha, N. Cowan, S. Domagal-Goldman, C. Dressing, Y. Fujii, R. Kopparapu, A. Lincowski, E. Lopez, J. Lustig-Yaeger, and A. Youngblood. The Importance of Multiple Observation Methods to Characterize Potentially Habitable Exoplanets: Ground- and Space-Based Synergies. *ArXiv e-prints*, March 2018.

[4] R. Barnes. Tidal locking of habitable exoplanets. *Celestial Mechanics and Dynamical Astronomy*, 129:509–536, December 2017.

[5] N. Batalha, J. Kalirai, J. Lunine, M. Clampin, and D. Lindler. Transiting Exoplanet Simulations with the James Webb Space Telescope. *ArXiv e-prints*, July 2015.

[6] N. E. Batalha, E. M.-R. Kempton, and R. Mbarek. Challenges to Constraining Exoplanet Masses via Transmission Spectroscopy. *The Astrophysical Journal Letters*, 836:L5, February 2017.

[7] N. M. Batalha. Exploring exoplanet populations with NASA's Kepler Mission. *Proceedings of the National Academy of Science*, 111:12647–12654, September 2014.

[8] M. R. Bate. Stellar, brown dwarf and multiple star properties from hydrodynamical simulations of star cluster formation. *Monthly Notices of the Royal Astronomical Society*, 392:590–616, January 2009.

[9] C. Beichman, B. Benneke, H. Knutson, R. Smith, C. Dressing, D. Latham, D. Deming, J. Lunine, P.-O. Lagage, A. Sozzetti, C. Beichman, D. Sing,

E. Kempton, G. Ricker, J. Bean, L. Kreidberg, J. Bouwman, I. Crossfield, J. Christiansen, D. Ciardi, J. Fortney, L. Albert, R. Doyon, M. Rieke, G. Rieke, M. Clampin, M. Greenhouse, P. Goudfrooij, D. Hines, T. Keyes, J. Lee, P. McCullough, M. Robberto, J. Stansberry, J. Valenti, P. D. Deroo, A. Mandell, M. E. Ressler, A. Shporer, M. Swain, G. Vasisht, S. Carey, J. Krick, S. Birkmann, P. Ferruit, G. Giardino, T. Greene, and S. Howell. Observations of Transiting Exoplanets with the James Webb Space Telescope (JWST), Publications of the Astronomical Society of the Pacific (PASP), December 2014. *ArXiv e-prints*, November 2014.

[10] E. Bendek, M. Ammons, D. Bennett, J. Breckinridge, O. Guyon, A. Gould, H. Hildebrandt, V. Makarov, F. Malbet, M. Shao, J. Sahlmann, A. Sozzetti, and D. Spergel. Astrometry for exoplanet detection. UV-VIS-APRA Workshop presentation, 2015.

[11] H. Beust, M. Bonnefoy, A.-L. Maire, D. Ehrenreich, A.-M. Lagrange, and G. Chauvin. Orbital fitting of imaged planetary companions with high eccentricities and unbound orbits. Their application to Fomalhaut b and PZ Telecopii B. *Astronomy and Astrophysics*, 587:A89, March 2016.

[12] B. A. Biller and M. Bonnefoy. *Exoplanet Atmosphere Measurements from Direct Imaging*, page 101. 2017.

[13] W. J. Borucki, D. G. Koch, G. Basri, N. Batalha, T. M. Brown, S. T. Bryson, D. Caldwell, J. Christensen-Dalsgaard, W. D. Cochran, E. DeVore, E. W. Dunham, T. N. Gautier, III, J. C. Geary, R. Gilliland, A. Gould, S. B. Howell, J. M. Jenkins, D. W. Latham, J. J. Lissauer, G. W. Marcy, J. Rowe, D. Sasselov, A. Boss, D. Charbonneau, D. Ciardi, L. Doyle, A. K. Dupree, E. B. Ford, J. Fortney, M. J. Holman, S. Seager, J. H. Steffen, J. Tarter, W. F. Welsh, C. Allen, L. A. Buchhave, J. L. Christiansen, B. D. Clarke, S. Das, J.-M. Désert, M. Endl, D. Fabrycky, F. Fressin, M. Haas, E. Horch, A. Howard, H. Isaacson, H. Kjeldsen, J. Kolodziejczak, C. Kulesa, J. Li, P. W. Lucas, P. Machalek, D. McCarthy, P. MacQueen, S. Meibom, T. Miquel, A. Prsa, S. N. Quinn, E. V. Quintana, D. Ragozzine, W. Sherry, A. Shporer, P. Tenenbaum, G. Torres, J. D. Twicken, J. Van Cleve, L. Walkowicz, F. C. Witteborn, and M. Still. Characteristics of Planetary Candidates Observed by Kepler. II. Analysis of the First Four Months of Data. *The Astrophysical Journal*, 736:19, July 2011.

[14] William J. Borucki, David Koch, Gibor Basri, Natalie Batalha, Timothy Brown, Douglas Caldwell, John Caldwell, Jørgen Christensen-Dalsgaard, William D. Cochran, Edna DeVore, Edward W. Dunham, Andrea K. Dupree, Thomas N. Gautier, John C. Geary, Ronald Gilliland, Alan Gould, Steve B. Howell, Jon M. Jenkins, Yoji Kondo, David W. Latham, Geoffrey W. Marcy, Søren Meibom, Hans Kjeldsen, Jack J. Lissauer, David G. Monet, David Morrison, Dimitar Sasselov, Jill Tarter, Alan Boss, Don Brownlee, Toby Owen, Derek Buzasi, David Charbonneau, Laurance Doyle, Jonathan Fortney, Eric B. Ford, Matthew J. Holman, Sara Seager, Jason H. Steffen, William F. Welsh, Jason Rowe, Howard Anderson, Lars Buchhave, David Ciardi, Lucianne Walkowicz, William Sherry, Elliott Horch, Howard Isaacson, Mark E. Everett, Debra Fischer, Guillermo Torres, John Asher Johnson, Michael Endl, Phillip MacQueen, Stephen T. Bryson, Jessie Dotson, Michael Haas, Jeffrey Kolodziejczak, Jeffrey Van Cleve, Hema Chandrasekaran, Joseph D. Twicken, Elisa V. Quintana, Bruce D. Clarke, Christopher Allen, Jie Li, Haley Wu, Peter Tenenbaum, Ekaterina Verner, Frederick Bruhweiler, Jason Barnes, and Andrej Prsa. Kepler planet-detection mission: Introduction and first results. *Science*, 327(5968):977–980, 2010.

[15] J. Bovy. Stellar inventory of the solar neighbourhood using Gaia DR1. *Monthly Notices of the Royal Astronomical Society*, 470:1360–1387, September 2017.

[16] B. P. Bowler. Imaging Extrasolar Giant Planets. *Publications of the Astronomical Society of the Pacific*, 128(10):102001, October 2016.

[17] R. A. Brown. Single-Visit Photometric and Obscurational Completeness. *The Astrophysical Journal*, 624:1010–1024, May 2005.

[18] L. A. Buchhave, C. D. Dressing, X. Dumusque, K. Rice, A. Vanderburg, A. Mortier, M. Lopez-Morales, E. Lopez, M. S. Lundkvist, H. Kjeldsen, L. Affer, A. S. Bonomo, D. Charbonneau, A. Collier Cameron, R. Cosentino, P. Figueira, A. F. M. Fiorenzano, A. Harutyunyan, R. D. Haywood, J. A. Johnson, D. W. Latham, C. Lovis, L. Malavolta, M. Mayor, G. Micela, E. Molinari, F. Motalebi, V. Nascimbeni, F. Pepe, D. F. Phillips, G. Piotto, D. Pollacco, D. Queloz, D. Sasselov, D. Ségransan, A. Sozzetti, S. Udry, and C. Watson. A 1.9 Earth Radius Rocky Planet and the Discovery of a Non-transiting Planet in the Kepler-20 System. *The Astronomical Journal*, 152:160, December 2016.

[19] C. J. Burke, J. L. Christiansen, F. Mullally, S. Seader, D. Huber, J. F. Rowe, J. L. Coughlin, S. E. Thompson, J. Catanzarite, B. D. Clarke, T. D. Morton, D. A. Caldwell, S. T. Bryson, M. R. Haas, N. M. Batalha, J. M. Jenkins, P. Tenenbaum, J. D. Twicken, J. Li, E. Quintana, T. Barclay, C. E. Henze, W. J. Borucki, S. B. Howell, and M. Still. Terrestrial Planet Occurrence Rates for the Kepler GK Dwarf Sample. *The Astrophysical Journal*, 809:8, August 2015.

[20] A. Burrows and G. Orton. *Giant Planet Atmospheres and Spectra*. October 2009.

[21] R. P. Butler, S. S. Vogt, G. Laughlin, J. A. Burt, E. J. Rivera, M. Tuomi, J. Teske, P. Arriagada, M. Diaz, B. Holden, and S. Keiser. The LCES HIRES/Keck Precision Radial Velocity Exoplanet Survey. *The Astronomical Journal*, 153:208, May 2017.

[22] K. L. Cahoy, M. S. Marley, and J. J. Fortney. Exoplanet Albedo Spectra and Colors as a Function of Planet Phase, Separation, and Metallicity. *The Astrophysical Journal*, 724:189–214, November 2010.

[23] J. Catanzarite and M. Shao. The Occurrence Rate of Earth Analog Planets Orbiting Sun-like Stars. *The Astrophysical Journal*, 738:151, September 2011.

[24] J. Chen and D. Kipping. Probabilistic Forecasting of the Masses and Radii of Other Worlds. *The Astrophysical Journal*, 834:17, January 2017.

[25] J. L. Christiansen. Exoplanet Catalogues. *ArXiv e-prints*, March 2018.

[26] J. L. Christiansen, B. D. Clarke, C. J. Burke, S. Seader, J. M. Jenkins, J. D. Twicken, J. D. Catanzarite, J. C. Smith, N. M. Batalha, M. R. Haas, S. E. Thompson, J. R. Campbell, A. Sabale, and A. Kamal Uddin. Measuring Transit Signal Recovery in the Kepler Pipeline II: Detection Efficiency as Calculated in One Year of Data. *The Astrophysical Journal*, 810:95, September 2015.

[27] N. B. Cowan. Water On -and In- Terrestrial Planets. *ArXiv e-prints*, November 2015.

[28] N. B. Cowan, E. Agol, V. S. Meadows, T. Robinson, T. A. Livengood, D. Deming, C. M. Lisse, M. F. A'Hearn, D. D. Wellnitz, S. Seager, D. Charbonneau, and EPOXI Team. Alien Maps of an Ocean-bearing World. *The Astrophysical Journal*, 700:915–923, August 2009.

[29] N. B. Cowan, P. A. Fuentes, and H. M. Haggard. Light curves of stars and exoplanets: estimating inclination, obliquity and albedo. *Monthly Notices of the Royal Astronomical Society*, 434:2465–2479, September 2013.

[30] N. B. Cowan and Y. Fujii. Mapping Exoplanets. *ArXiv e-prints*, April 2017.

[31] N. B. Cowan, T. Greene, D. Angerhausen, N. E. Batalha, M. Clampin, K. Colón, I. J. M. Crossfield, J. J. Fortney, B. S. Gaudi, J. Harrington, N. Iro, C. F. Lillie, J. L. Linsky, M. Lopez-Morales, A. M. Mandell, and K. B. Stevenson. Characterizing Transiting Planet Atmospheres through 2025. *Publications of the Astronomical Society of the Pacific*, 127:311, March 2015.

[32] C. A. Crow, L. A. McFadden, T. Robinson, V. S. Meadows, T. A. Livengood, T. Hewagama, R. K. Barry, L. D. Deming, C. M. Lisse, and D. Wellnitz. Views from EPOXI: Colors in Our Solar System as an Analog for Extrasolar Planets. *The Astrophysical Journal*, 729:130, March 2011.

[33] A. Cumming. *Statistical Distribution of Exoplanets*. 2010.

[34] A. Cumming, R. P. Butler, G. W. Marcy, S. S. Vogt, J. T. Wright, and D. A. Fischer. The Keck Planet Search: Detectability and the Minimum Mass and Orbital Period Distribution of Extrasolar Planets. *Publications of the Astronomical Society of the Pacific*, 120:531, May 2008.

[35] J. Dalcanton, S. Seager, S. Aigrain, S. Battel, N. Brandt, C. Conroy, L. Feinberg, S. Gezari, O. Guyon, W. Harris, C. Hirata, J. Mather, M. Postman, D. Redding, D. Schiminovich, H. P. Stahl, and J. Tumlinson. From Cosmic Birth to Living Earths: The Future of UVOIR Space Astronomy. *ArXiv e-prints*, July 2015.

[36] J. de Wit and S. Seager. Constraining Exoplanet Mass from Transmission Spectroscopy. *Science*, 342:1473–1477, December 2013.

[37] D. Deming and S. Seager. Illusion and Reality in the Atmospheres of Exoplanets. *ArXiv e-prints*, January 2017.

[38] S. Dong and Z. Zhu. Fast Rise of "Neptune-size" Planets from P 10 to 250 Days—Statistics of Kepler Planet Candidates up to 0.75 AU. *The Astrophysical Journal*, 778:53, November 2013.

[39] J. Dooley and P. Lawson. Technology Plan for the Terrestrial Planet Finder Coronagraph. Technical Report 05-8, Jet Propulsion Laboratory, California Institute of Technology, March 2005.

[40] B. Farr, W. M. Farr, N. B. Cowan, H. M. Haggard, and T. Robinson. exocartographer: A Bayesian Framework for Mapping Exoplanets in Reflected Light. *ArXiv e-prints*, February 2018.

[41] Y. K. Feng, T. D. Robinson, J. J. Fortney, R. E. Lupu, M. S. Marley, N. K. Lewis, B. Macintosh, and M. R. Line. Characterizing Earth Analogs in Reflected Light: Atmospheric Retrieval Studies for Future Space Telescopes. *ArXiv e-prints*, March 2018.

[42] D. A. Fischer, G. Anglada-Escude, P. Arriagada, R. V. Baluev, J. L. Bean, F. Bouchy, L. A. Buchhave, T. Carroll, A. Chakraborty, J. R. Crepp, R. I. Dawson, S. A. Diddams, X. Dumusque, J. D. Eastman, M. Endl, P. Figueira, E. B. Ford, D. Foreman-Mackey, P. Fournier, G. Fűrész, B. S. Gaudi, P. C. Gregory, F. Grundahl, A. P. Hatzes, G. Hébrard, E. Herrero, D. W. Hogg, A. W. Howard, J. A. Johnson, P. Jorden, C. A. Jurgenson, D. W. Latham, G. Laughlin, T. J. Loredo, C. Lovis, S. Mahadevan, T. M. McCracken, F. Pepe, M. Perez, D. F. Phillips, P. P. Plavchan, L. Prato, A. Quirrenbach, A. Reiners, P. Robertson, N. C. Santos, D. Sawyer, D. Segransan, A. Sozzetti, T. Steinmetz, A. Szentgyorgyi, S. Udry, J. A. Valenti, S. X. Wang, R. A. Wittenmyer, and J. T. Wright. State of the Field: Extreme Precision Radial Velocities. *Publications of the Astronomical Society of the Pacific*, 128(6):066001, June 2016.

[43] E. B. Ford. Improving the Efficiency of Markov Chain Monte Carlo for Analyzing the Orbits of Extrasolar Planets. *The Astrophysical Journal*, 642:505–522, May 2006.

[44] E. B. Ford, S. Seager, and E. L. Turner. Characterization of extrasolar terrestrial planets from diurnal photometric variability. *Nature*, 412:885 EP –, 08 2001.

[45] D. Foreman-Mackey, D. W. Hogg, and T. D. Morton. Exoplanet Population Inference and the Abundance of Earth Analogs from Noisy, Incomplete Catalogs. *The Astrophysical Journal*, 795:64, November 2014.

[46] J. Fraine, D. Deming, B. Benneke, H. Knutson, A. Jordán, N. Espinoza, N. Madhusudhan, A. Wilkins, and K. Todorov. Water vapour absorption in the clear atmosphere of a Neptune-sized exoplanet. *Nature*, 513:526–529, September 2014.

[47] F. Fressin, G. Torres, D. Charbonneau, S. T. Bryson, J. Christiansen, C. D. Dressing, J. M. Jenkins, L. M. Walkowicz, and N. M. Batalha. The False Positive Rate of Kepler and the Occurrence of Planets. *The Astrophysical Journal*, 766:81, April 2013.

[48] Y. Fujii and H. Kawahara. Mapping Earth Analogs from Photometric Variability: Spin-Orbit Tomography for Planets in Inclined Orbits. *The Astrophysical Journal*, 755:101, August 2012.

[49] Y. Fujii, J. Lustig-Yaeger, and N. B. Cowan. Rotational Spectral Unmixing of Exoplanets: Degeneracies between Surface Colors and Geography. *The Astronomical Journal*, 154:189, November 2017.

[50] B. J. Fulton, E. A. Petigura, A. W. Howard, H. Isaacson, G. W. Marcy, P. A. Cargile, L. Hebb, L. M. Weiss, J. A. Johnson, T. D. Morton, E. Sinukoff, I. J. M. Crossfield, and L. A. Hirsch. The California-Kepler Survey. III. A Gap in the Radius Distribution of Small Planets. *The Astronomical Journal*, 154:109, September 2017.

[51] A. García Muñoz, P. Lavvas, and R. A. West. Titan brighter at twilight than in daylight. *Nature Astronomy*, 1:0114, April 2017.

[52] B. S. Gaudi and ExoPAG. Exoplanet exploration program analysis group (exopag) report to paul hertz regarding large mission concepts to study for the 2020 decadal survey. Technical report, NASA/GSFC, 2015.

[53] B. S. Gaudi and Habitable Exoplanet Imaging Mission Science and Technology Definition Team. The Habitable Exoplanet (HabEx) Imaging Mission: Preliminary Science Drivers and Technical Requirements. In *American Astronomical Society Meeting Abstracts no. 229*, volume 229 of *American Astronomical Society Meeting Abstracts*, page 405.02, January 2017.

[54] C. Ginski, T. O. B. Schmidt, M. Mugrauer, R. Neuhäuser, N. Vogt, R. Ermann, and A. Berndt. Astrometric follow-up observations of directly imaged sub-stellar companions to young stars and brown dwarfs. *Monthly Notices of the Royal Astronomical Society*, 444:2280–2302, November 2014.

[55] S. Ginzburg, H. E. Schlichting, and R. Sari. Core-powered mass-loss and the radius distribution of small exoplanets. *Monthly Notices of the Royal Astronomical Society*, 476:759–765, May 2018.

[56] C. Goldblatt. Atmospheric Evolution. *ArXiv e-prints*, October 2017.

[57] C. M. Guimond and N. B. Cowan. The direct imaging search for Earth 2.0: Quantifying biases and planetary false positives. *ArXiv e-prints*, April 2018.

[58] O. Guyon. High performance coronagraphy for direct imaging of exoplanets. In *European Physical Journal Web of Conferences*, volume 16 of *European Physical Journal Web of Conferences*, page 03001, July 2011.

[59] R. Heller, J. Leconte, and R. Barnes. Tidal obliquity evolution of potentially habitable planets. *Astronomy & Astrophysics*, 528:A27, April 2011.

[60] K. Heng and B.-O. Demory. Understanding Trends Associated with Clouds in Irradiated Exoplanets. *The Astrophysical Journal*, 777:100, November 2013.

[61] D. C. Hsu, E. B. Ford, D. Ragozzine, and R. C. Morehead. Improving the Accuracy of Planet Occurrence Rates from Kepler using Approximate Bayesian Computation. *ArXiv e-prints*, March 2018.

[62] A. R. Iyer, M. R. Swain, R. T. Zellem, M. R. Line, G. Roudier, G. Rocha, and J. H. Livingston. A Characteristic Transmission Spectrum Dominated by H_2O Applies to the Majority of HST/WFC3 Exoplanet Observations. *The Astrophysical Journal*, 823:109, June 2016.

[63] L. Kaltenegger and W. A. Traub. Transits of Earth-like Planets. *The Astrophysical Journal*, 698:519–527, June 2009.

[64] J. F. Kasting, D. P. Whitmire, and R. T. Reynolds. Habitable Zones around Main Sequence Stars. *Icarus*, 101:108–128, January 1993.

[65] James F. Kasting, Ravikumar Kopparapu, Ramses M. Ramirez, and Chester E. Harman. Remote life-detection criteria, habitable zone boundaries, and the frequency of earth-like planets around m and late k stars. *Proceedings of the National Academy of Sciences*, 111(35):12641–12646, 2014.

[66] H. Kawahara and Y. Fujii. Global Mapping of Earth-like Exoplanets From Scattered Light Curves. *The Astrophysical Journal*, 720:1333–1350, September 2010.

[67] H. Kawahara and Y. Fujii. Mapping Clouds and Terrain of Earth-like Planets from Photometric Variability: Demonstration with Planets in Face-on Orbits. *The Astrophysical Journal Letters*, 739:L62, October 2011.

[68] E. S. Kite, E. Gaidos, and M. Manga. Climate Instability on Tidally Locked Exoplanets. *The Astrophysical Journal*, 743:41, December 2011.

[69] R. Kopparapu, E. Hebrard, R. Belikov, N. M. Batalha, G. D. Mulders, C. Stark, D. Teal, S. Domagal-Goldman, D. Gelino, A. Mandell, A. Roberge, S. Rinehart, S. R. Kane, Y. Hasegawa, W. Henning, B. Hicks, V. Adibekyan, E. W. Schwieterman, E. Kohler, J. Teske, N. Hinkel, C. Nixon, K. France, W. Danchi, J. Haqq-Misra, E. T. Wolf, S. D. Guzewich, B. Charnay, G. Arney, H. E. Hartnett, E. D. Lopez, D. Minniti, J. Renaud, V. Airapetian, C. Dong, A. D. Del Genio, M. Trainer, G. Rau, A. Jensen, M. Way, C. M. Lisse, W. Lyra, F. Marchis, D. Jontof-Hutter, P. Young, R. Pierrehumbert, C. E. Harman, J. Fortney, B. Moore, S. Beckwith, E. Shock, S. Desch, K. E. Mandt, N. Izenberg, E. B. Ford, S. Curry, C. Scharf, and A. Anbar. Exoplanet Diversity in the Era of Space-based Direct Imaging Missions. *ArXiv e-prints*, March 2018.

[70] R. k. Kopparapu, E. Hebrard, R. Belikov, N. M. Batalha, G. D. Mulders, C. Stark, D. Teal, S. Domagal-Goldman, and A. Mandell. Exoplanet Classification and Yield Estimates for Direct Imaging Missions. *ArXiv e-prints*, February 2018.

[71] R. K. Kopparapu, R. Ramirez, J. F. Kasting, V. Eymet, T. D. Robinson, S. Mahadevan, R. C. Terrien, S. Domagal-Goldman, V. Meadows, and R. Deshpande. Habitable Zones around Main-sequence Stars: New Estimates. *The Astrophysical Journal*, 765:131, March 2013.

[72] R. K. Kopparapu, E. T. Wolf, J. Haqq-Misra, J. Yang, J. F. Kasting, V. Meadows, R. Terrien, and S. Mahadevan. The Inner Edge of the Habitable Zone for Synchronously Rotating Planets around Low-mass Stars Using General Circulation Models. *The Astrophysical Journal*, 819:84, March 2016.

[73] J. Krissansen-Totton, E. W. Schwieterman, B. Charnay, G. Arney, T. D. Robinson, V. Meadows, and D. C. Catling. Is the Pale Blue Dot Unique? Optimized Photometric Bands for Identifying Earth-like Exoplanets. *The Astrophysical Journal*, 817:31, January 2016.

[74] P. Kroupa and A. Burkert. On the Origin of the Distribution of Binary Star Periods. *The Astrophysical Journal*, 555:945–949, July 2001.

[75] Anne-Marie Lagrange. Direct imaging of exoplanets. *Philosophical Transactions of the Royal Society of London A: Mathematical, Physical and Engineering Sciences*, 372(2014), 2014.

[76] J. Lannier, A. M. Lagrange, M. Bonavita, S. Borgniet, P. Delorme, N. Meunier, S. Desidera, S. Messina, G. Chauvin, and M. Keppler. Combining direct imaging and radial velocity data towards a full exploration of the giant planet population. I. Method and first results. *Astronomy and Astrophysics*, 603:A54, July 2017.

[77] E. J. Lee, E. Chiang, and J. W. Ferguson. Optically Thin Core Accretion: How Planets Get Their Gas in Nearly Gas-Free Disks. *ArXiv e-prints*, October 2017.

[78] O. R. Lehmer and D. C. Catling. Rocky Worlds Limited to $\sim$1.8 Earth Radii by Atmospheric Escape during a Star's Extreme UV Saturation. *The Astrophysical Journal*, 845:130, August 2017.

[79] M. Lingam and A. Loeb. Physical constraints on the likelihood of life on exoplanets. *International Journal of Astrobiology*, 17:116–126, April 2018.

[80] E. D. Lopez and J. J. Fortney. Understanding the Mass-Radius Relation for Sub-neptunes: Radius as a Proxy for Composition. *The Astrophysical Journal*, 792:1, September 2014.

[81] E. D. Lopez and K. Rice. Predictions for the Period Dependence of the Transition Between Rocky Super-Earths and Gaseous Sub-Neptunes and Implications for $\eta\_\oplus$. *ArXiv e-prints*, October 2016.

[82] B. Macintosh, J. R. Graham, P. Ingraham, Q. Konopacky, C. Marois, M. Perrin, L. Poyneer, B. Bauman, T. Barman, A. S. Burrows, A. Cardwell, J. Chilcote, R. J. De Rosa, D. Dillon, R. Doyon, J. Dunn, D. Erikson, M. P. Fitzgerald, D. Gavel, S. Goodsell, M. Hartung, P. Hibon, P. Kalas, J. Larkin, J. Maire, F. Marchis, M. S. Marley, J. McBride, M. Millar-Blanchaer, K. Morzinski, A. Norton, B. R. Oppenheimer, D. Palmer, J. Patience, L. Pueyo, F. Rantakyro, N. Sadakuni, L. Saddlemyer, D. Savransky, A. Serio, R. Soummer, A. Sivaramakrishnan, I. Song, S. Thomas, J. K. Wallace, S. Wiktorowicz, and S. Wolff. First light of the Gemini Planet Imager. *Proceedings of the National Academy of Science*, 111:12661–12666, September 2014.

[83] David J. Des Marais, Martin O. Harwit, Kenneth W. Jucks, James F. Kasting, Douglas N. C. Lin, Jonathan I. Lunine, Jean Schneider, Sara Seager, Wesley A. Traub, and Neville J. Woolf. Remote sensing of planetary properties and biosignatures on extrasolar terrestrial planets. *Astrobiology*, 2 2:153–81, 2002.

[84] C. H. Mayer, T. P. McCullough, and R. M. Sloanaker. Observations of Venus at 3.15-CM Wave Length. *The Astrophysical Journal*, 127:1, January 1958.

[85] L. C. Mayorga, J. Jackiewicz, K. Rages, R. A. West, B. Knowles, N. Lewis, and M. S. Marley. Jupiter's Phase Variations from Cassini: A Testbed for Future Direct-imaging Missions. *The Astronomical Journal*, 152:209, December 2016.

[86] V. S. Meadows. personal communication.

[87] M. F. Michael F. Sterzik, S. Bagnulo, and E. Pallé. Biosignatures as revealed by spectropolarimetry of Earthshine. *Nature*, 483:64–66, March 2012.

[88] E. Miller-Ricci, S. Seager, and D. Sasselov. The Atmospheric Signatures of Super-Earths: How to Distinguish Between Hydrogen-Rich and Hydrogen-Poor Atmospheres. *The Astrophysical Journal*, 690:1056–1067, January 2009.

[89] M. Nayak, R. Lupu, M. S. Marley, J. J. Fortney, T. Robinson, and N. Lewis. Atmospheric Retrieval for Direct Imaging Spectroscopy of Gas Giants in Reflected Light. II. Orbital Phase and Planetary Radius. *Publications of the Astronomical Society of the Pacific*, 129(3):034401, March 2017.

[90] B. Nelson, E. B. Ford, and M. J. Payne. RUN DMC: An Efficient, Parallel Code for Analyzing Radial Velocity Observations Using N-body Integrations and Differential Evolution Markov Chain Monte Carlo. *The Astrophysical Journal, Supplement*, 210:11, January 2014.

[91] L. Noack, A. Rivoldini, and T. Van Hoolst. Volcanism and outgassing of stagnant-lid planets: Implications for the habitable zone. *Physics of the Earth and Planetary Interiors*, 269:40–57, August 2017.

[92] P. H. H. Oakley and W. Cash. Construction of an Earth Model: Analysis of Exoplanet Light Curves and Mapping the Next Earth with the New Worlds Observer. *The Astrophysical Journal*, 700:1428–1439, August 2009.

[93] J. E. Owen and Y. Wu. The Evaporation Valley in the Kepler Planets. *The Astrophysical Journal*, 847:29, September 2017.

[94] E. Pallé, E. B. Ford, S. Seager, P. Montañés-Rodríguez, and M. Vazquez. Identifying the Rotation Rate and the Presence of Dynamic Weather on Extrasolar Earth-like Planets from Photometric Observations. *The Astrophysical Journal*, 676:1319–1329, April 2008.

[95] A. Paradise, K. Menou, D. Valencia, and C. Lee. Habitable Snowballs: Generalizing the Habitable Zone. *ArXiv e-prints*, March 2018.

[96] E. A. Petigura, A. W. Howard, and G. W. Marcy. Prevalence of Earth-size planets orbiting Sun-like stars. *Proceedings of the National Academy of Science*, 110:19273–19278, November 2013.

[97] P. Plavchan, B. Cale, P. Newman, B. Hamze, N. Latouf, W. Matzko, C. Beichman, D. Ciardi, B. Purcell, P. Lightsey, H. Cegla, X. Dumusque, V. Bourrier, C. Dressing, P. Gao, G. Vasisht, S. Leifer, S. Wang, J. Gagne, S. Thompson, J. Crass, A. Bechter, E. Bechter, C. Blake, S. Halverson, A. Mayo, T. Beatty, J. T Wright, A. Wise, A. Tanner, J. Eastman, S. Quinn, D. Fischer, S. Basu, S. Sanchez-Maes, A. Howard, K. Vahala, J. Wang, S. Diddams, S. Papp, B. J. Pope, E. Martin, and S. Murphy. EarthFinder: A Precise Radial Velocity Probe Mission Concept For the Detection of Earth-Mass Planets Orbiting Sun-like Stars. *ArXiv e-prints*, March 2018.

[98] L. Pueyo, R. Soummer, J. Hoffmann, R. Oppenheimer, J. R. Graham, N. Zimmerman, C. Zhai, J. K. Wallace, F. Vescelus, A. Veicht, G. Vasisht, T. Truong, A. Sivaramakrishnan, M. Shao, L. C. Roberts, Jr., J. E. Roberts,

E. Rice, I. R. Parry, R. Nilsson, T. Lockhart, E. R. Ligon, D. King, S. Hinkley, L. Hillenbrand, D. Hale, R. Dekany, J. R. Crepp, E. Cady, R. Burruss, D. Brenner, C. Beichman, and C. Baranec. Reconnaissance of the HR 8799 Exosolar System. II. Astrometry and Orbital Motion. *The Astrophysical Journal*, 803:31, April 2015.

[99] P. Ranalli, D. Hobbs, and L. Lindegren. Astrometry and exoplanets in the Gaia era: a Bayesian approach to detection and parameter recovery. *ArXiv e-prints*, April 2017.

[100] B. Rauscher, M. Bolcar, M. Clampin, S. Domagal-Goldman, M. McElwain, S. Moseley, C. Stahle, C. Stark, and H. Thronson. ATLAST Detector Needs for Direct Spectroscopic Biosignature Characterization in the Visible and Near-IR. In *Proc. SPIE Optics + Photonics 2015*. International Society for Optical Engineering, 2015.

[101] C. T. Reinhard, S. L. Olson, E. W. Schwieterman, and T. W. Lyons. False Negatives for Remote Life Detection on Ocean-Bearing Planets: Lessons from the Early Earth. *Astrobiology*, 17:287–297, April 2017.

[102] J. Rhodes, T. Meshkat, M. Frerking, B. Mennesson, M. Turnbull, B. Macintosh, and J. Kasdin. WFIRST: Discovery and characterization of planets in the habitable zone with the CGI. In *American Astronomical Society Meeting Abstracts no. 231*, volume 231 of *American Astronomical Society Meeting Abstracts*, page 158.02, January 2018.

[103] A. Roberge, C. H. Chen, R. Millan-Gabet, A. J. Weinberger, P. M. Hinz, K. R. Stapelfeldt, O. Absil, M. J. Kuchner, and G. Bryden. The Exozodiacal Dust Problem for Direct Observations of Exo-Earths. *Publications of the Astronomical Society of the Pacific*, 124:799, August 2012.

[104] A. Roberge, M. J. Rizzo, A. P. Lincowski, G. N. Arney, C. C. Stark, T. D. Robinson, G. F. Snyder, L. Pueyo, N. T. Zimmerman, T. Jansen, E. R. Nesvold, V. S. Meadows, and M. C. Turnbull. Finding the Needles in the Haystacks: High-fidelity Models of the Modern and Archean Solar System for Simulating Exoplanet Observations. *Publications of the Astronomical Society of the Pacific*, 129(12):124401, December 2017.

[105] T. D. Robinson, K. Ennico, V. S. Meadows, W. Sparks, D. B. J. Bussey, E. W. Schwieterman, and J. Breiner. Detection of Ocean Glint and Ozone

Absorption Using LCROSS Earth Observations. *The Astrophysical Journal*, 787:171, June 2014.

[106] T. D. Robinson and C. T. Reinhard. Earth as an Exoplanet. *ArXiv e-prints*, April 2018.

[107] T. D. Robinson, K. R. Stapelfeldt, and M. S. Marley. Characterizing Rocky and Gaseous Exoplanets with 2 m Class Space-based Coronagraphs. *Publications of the Astronomical Society of the Pacific*, 128(2):025003, February 2016.

[108] L. A. Rogers. Most 1.6 Earth-radius Planets are Not Rocky. *The Astrophysical Journal*, 801:41, March 2015.

[109] C. Sagan, W. R. Thompson, R. Carlson, D. Gurnett, and C. Hord. A search for life on Earth from the Galileo spacecraft. *Nature*, 365:715–721, October 1993.

[110] Carl Sagan. On the origin and planetary distribution of life. *Radiation Research*, 15(2):174–192, 1961.

[111] LUVOIR Science and Technology Definition Team. The luvoir interim report. Technical report, NASA/GSFC, 2018. draft version accessed January 2018.

[112] S. Seager, E. L. Turner, J. Schafer, and E. B. Ford. Vegetation's Red Edge: A Possible Spectroscopic Biosignature of Extraterrestrial Plants. *Astrobiology*, 5:372–390, June 2005.

[113] Sara Seager. The future of spectroscopic life detection on exoplanets. *Proceedings of the National Academy of Sciences*, 111(35):12634–12640, 2014.

[114] M. Shabram, B.-O. Demory, J. Cisewski, E. B. Ford, and L. Rogers. The Eccentricity Distribution of Short-period Planet Candidates Detected by Kepler in Occultation. *The Astrophysical Journal*, 820:93, April 2016.

[115] M. Shao, G. Marcy, J. H. Catanzarite, S. J. Edberg, A. Léger, F. Malbet, D. Queloz, M. W. Muterspaugh, C. Beichman, D. Fischer, E. Ford, R. Olling, S. Kulkarni, S. C. Unwin, and W. Traub. Astrometric Detection of Earthlike Planets. In *astro2010: The Astronomy and Astrophysics Decadal Survey*, volume 2010 of *Astronomy*, 2009.

[116] M. Shao, S. G. Turyshev, E. Bendek, D. Fischer, O. Guyon, B. McArthur, M. Muterspaugh, C. Zhai, and C. Boehm. Precision Space Astrometry as a Tool to Find Earth-like Exoplanets. *ArXiv e-prints*, March 2018.

[117] A. L. Shields, S. Ballard, and J. A. Johnson. The habitability of planets orbiting M-dwarf stars. *Physics Reports*, 663:1, December 2016.

[118] A. Silburt, E. Gaidos, and Y. Wu. A Statistical Reconstruction of the Planet Population around Kepler Solar-type Stars. *The Astrophysical Journal*, 799:180, February 2015.

[119] A. Sozzetti, M. Bonavita, S. Desidera, R. Gratton, and M. G. Lattanzi. Gaia: The Astrometry Revolution. In J. H. Kastner, B. Stelzer, and S. A. Metchev, editors, *Young Stars & Planets Near the Sun*, volume 314 of *IAU Symposium*, pages 264–269, January 2016.

[120] D. S. Spiegel, K. Menou, and C. A. Scharf. Habitable Climates. *The Astrophysical Journal*, 681:1609–1623, July 2008.

[121] C. C. Stark, A. Roberge, A. Mandell, M. Clampin, S. D. Domagal-Goldman, M. W. McElwain, and K. R. Stapelfeldt. Lower Limits on Aperture Size for an ExoEarth Detecting Coronagraphic Mission. *The Astrophysical Journal*, 808:149, August 2015.

[122] C. C. Stark, A. Roberge, A. Mandell, and T. D. Robinson. Maximizing the ExoEarth Candidate Yield from a Future Direct Imaging Mission. *The Astrophysical Journal*, 795:122, November 2014.

[123] C. C. Stark, Stuart B. Shaklan, Philip Douglas Lisman, Eric J. Cady, Dmitry Savransky, Aki Roberge, and Avi M. Mandell. Maximized exoearth candidate yields for starshades. *Journal of Astronomical Telescopes, Instruments, and Systems*, 2:2 – 2 – 17, 2016.

[124] W. A. Traub. The Colors of Extrasolar Planets. In D. Deming and S. Seager, editors, *Scientific Frontiers in Research on Extrasolar Planets*, volume 294 of *Astronomical Society of the Pacific Conference Series*, pages 595–602, 2003.

[125] W. A. Traub. Terrestrial, Habitable-zone Exoplanet Frequency from Kepler. *The Astrophysical Journal*, 745:20, January 2012.

[126] W. A. Traub and B. R. Oppenheimer. Direct Imaging of Exoplanets. In S. Seager, editor, *Exoplanets*, pages 111–156. December 2010.

[127] A. Vigan, M. Bonavita, B. Biller, D. Forgan, K. Rice, G. Chauvin, S. Desidera, J.-C. Meunier, P. Delorme, J. E. Schlieder, M. Bonnefoy, J. Carson, E. Covino, J. Hagelberg, T. Henning, M. Janson, A.-M. Lagrange, S. P. Quanz, A. Zurlo, J.-L. Beuzit, A. Boccaletti, E. Buenzli, M. Feldt, J. H. V. Girard, R. Gratton, M. Kasper, H. Le Coroller, D. Mesa, S. Messina, M. Meyer, G. Montagnier, C. Mordasini, D. Mouillet, C. Moutou, M. Reggiani, D. Segransan, and C. Thalmann. The VLT/NaCo large program to probe the occurrence of exoplanets and brown dwarfs at wide orbits. IV. Gravitational instability rarely forms wide, giant planets. *Astronomy and Astrophysics*, 603:A3, June 2017.

[128] A. Vigan, M. Bonnefoy, C. Ginski, H. Beust, R. Galicher, M. Janson, J.-L. Baudino, E. Buenzli, J. Hagelberg, V. D'Orazi, S. Desidera, A.-L. Maire, R. Gratton, J.-F. Sauvage, G. Chauvin, C. Thalmann, L. Malo, G. Salter, A. Zurlo, J. Antichi, A. Baruffolo, P. Baudoz, P. Blanchard, A. Boccaletti, J.-L. Beuzit, M. Carle, R. Claudi, A. Costille, A. Delboulbé, K. Dohlen, C. Dominik, M. Feldt, T. Fusco, L. Gluck, J. Girard, E. Giro, C. Gry, T. Henning, N. Hubin, E. Hugot, M. Jaquet, M. Kasper, A.-M. Lagrange, M. Langlois, D. Le Mignant, M. Llored, F. Madec, P. Martinez, D. Mawet, D. Mesa, J. Milli, D. Mouillet, T. Moulin, C. Moutou, A. Origné, A. Pavlov, D. Perret, C. Petit, J. Pragt, P. Puget, P. Rabou, S. Rochat, R. Roelfsema, B. Salasnich, H.-M. Schmid, A. Sevin, R. Siebenmorgen, A. Smette, E. Stadler, M. Suarez, M. Turatto, S. Udry, F. Vakili, Z. Wahhaj, L. Weber, and F. Wildi. First light of the VLT planet finder SPHERE. I. Detection and characterization of the substellar companion GJ 758 B. *Astronomy and Astrophysics*, 587:A55, March 2016.

[129] L. M. Weiss and G. W. Marcy. The Mass-Radius Relation for 65 Exoplanets Smaller than 4 Earth Radii. *The Astrophysical Journal Letters*, 783:L6, March 2014.

[130] L. M. Weiss, L. A. Rogers, H. T. Isaacson, E. Agol, G. W. Marcy, J. F. Rowe, D. Kipping, B. J. Fulton, J. J. Lissauer, A. W. Howard, and D. Fabrycky. Revised Masses and Densities of the Planets around Kepler-10. *The Astrophysical Journal*, 819:83, March 2016.

[131] J. N. Winn and D. C. Fabrycky. The Occurrence and Architecture of Exoplanetary Systems. *Annual Review of Astronomy and Astrophysics*, 53:409–447, August 2015.

[132] A. Wolszczan and D. A. Frail. A planetary system around the millisecond pulsar PSR1257 + 12. *Nature*, 355:145–147, January 1992.

[133] N. J. Woolf, P. S. Smith, W. A. Traub, and K. W. Jucks. The Spectrum of Earthshine: A Pale Blue Dot Observed from the Ground. *The Astrophysical Journal*, 574:430–433, July 2002.

[134] J. Yang, G. Boué, D. C. Fabrycky, and D. S. Abbot. Strong Dependence of the Inner Edge of the Habitable Zone on Planetary Rotation Rate. *The Astrophysical Journal Letters*, 787:L2, May 2014.

[135] A. N. Youdin. The Exoplanet Census: A General Method Applied to Kepler. *The Astrophysical Journal*, 742:38, November 2011.

[136] K. J. Zahnle and D. C. Catling. The Cosmic Shoreline: The Evidence that Escape Determines which Planets Have Atmospheres, and what this May Mean for Proxima Centauri B. *The Astrophysical Journal*, 843:122, July 2017.

[137] L. Zeng, S. B. Jacobsen, and D. D. Sasselov. Exoplanet Radius Gap Dependence on Host Star Type. *ArXiv e-prints*, December 2017.

List of mission and instrument abbreviations

GPI: Gemini Planet Imager

HabEx: Habitable Exoplanet Imaging Mission

JWST: James Webb Space Telescope

LUVOIR: The Large UltraViolet Optical Infrared Surveyor

SPHERE: Spectro-Polarimetric High-contrast Exoplanet Research instrument

WFIRST: Wide Field Infrared Survey Telescope